Journal of Applied Fluid Mechanics, Vol. 18, No. 5, pp. 1312-1334, 2025.
Available online at www.jafmonline.net, ISSN 1735-3572, EISSN 1735-3645.
https://doi.org/10.47176/jafm.18.5.2987

Experiment and Numerical Simulation of Aerodynamic Performance of Compressor with Damaged Blades

H. Sun[1†], Z. Wang[1,3] and G. Luo[2,3]

[1] *College of Energy and Power Engineering, Nanjing University of Aeronautics and Astronautics, Nanjing, Jiangsu, 210016, China*
[2] *State Key Laboratory of Mechanics and Control for Aerospace Structures, Nanjing University of Aeronautics and Astronautics, Nanjing, Jiangsu, 210016, China*
[3] *Liaoning Key Laboratory of Impact Dynamics on Aero Engine, Shenyang, Liaoning, 110015, China*

†*Corresponding Author Email: sh220@nuaa.edu.cn*

ABSTRACT

The present work attempted to lay a basis for evaluating the compressor aerodynamic performance in service environments. To achieve this goal, a low-speed compressor along with a transonic compressor rotor (NASA Rotor37) were studied. Different damaged blades were established, and three-dimensional viscous flow field simulations were accomplished. The influence of blade damage and the mechanism through which blade damage affects the compressor aerodynamic properties were analyzed. Further, the established numerical method was validated through low-speed compressor experiments. The results showed high resemblance of the simulations to the experimental findings, thus proving the effectiveness of our numerical simulation method. After the blade was damaged, the surge point of the compressor was advanced, the stable working flow range was reduced, and the aerodynamic performance was significantly reduced. The local airflow separation caused by the attack angle enlargement due to the deformation of blade after damage was the primary reason for the whole row of rotors to enter an unstable state. Unlike low-speed compressor, the rotor blade damage of transonic compressor caused the interference of shock wave with the boundary layer separation, and the burst low-speed region blocked the blade channel. This deteriorated the rotor flow state and caused greater flow loss, resulting in a more severe decline in the aerodynamic performance. The proposed numerical simulation approach for aerodynamic performance can effectively predict the steady-state aerodynamic performances of compressors with damaged blades.

Article History

Received July 11, 2024
Revised December 23, 2024
Accepted December 27, 2024
Available online March 4, 2025

Keywords:

Damaged blade
Compressor
Aerodynamic performance
Boundary layer separation
Shock wave

1. INTRODUCTION

Aerodynamic performance and internal flow state of compressor, as one of the three key aero-engine components, exert a pivotal effect on the stability and overall performance of aero-engines (Guan et al., 2007; Zhao et al., 2020; Sun et al., 2024). Recently, owing to the development of high-speed and large-scale airplanes, the performances of aero-engine compressors have been significantly improved. However, this has brought many challenges, such as the increase in the engine windward area, which has led to an increasing chance of swallowing of external objects (Li et al., 2024). Due to the large loads on compressor blades and the high tangential velocity at the blade tips, the combination of aerodynamic and centrifugal forces can easily cause significant geometric deformation when foreign objects are ingested by the high-speed rotating blades (Chen et al. 2023). This makes the middle to tip regions of the blades more prone to structural damage. Additionally, the blades have relatively thin leading edge, making it less capable of withstanding impact forces. As a result, damage to the leading edge upper-middle portion is most common, which accounts for approximately 70% of the total blade damage according to existing statistics. Therefore, in this study, damaged blades were constructed based on this observation. Considering the importance of compressor blades as critical components of the compressor, even minor geometric changes can significantly affect the compressor performance, leading to engine performance degradation or even loss of thrust. Consequently, scholars worldwide have conducted studies on the aerodynamic performances of damaged blades.

Venkatesh et al. (2020) studied the influence of blade leading edge damage over the aerodynamic properties of

NOMENCLATURE

SM	stability margin	π^*	total pressure ratio
$\dot{m}$	flow rate	s	near-instability condition
d	design condition	Φ_{tt}	total pressure rise coefficient
P_2^*	average absolute total pressure values of rotor outlet	P_1^*	average absolute total pressure values of rotor inlet
ρ	inlet density	U_m	rim speed
$\overline{\omega}$	loss coefficient	P_1	average static pressure of inlet
P_{1w}^*	average relative total pressure values of rotor inlet	P_{2w}^*	average relative total pressure values of rotor outlet

a first-stage transonic compressor. They found that blade chordal damage affects the stall boundary more than radial damage and that the degree of blade damage affects the compressor aerodynamic properties more than the number of damaged blades. Imregun and Vahdati (1999) explored the aeroelastic stability problem for an artificially assumed bird-impact-damaged blade by computational fluid dynamics (CFD) coupled with finite element modeling (FEM) simulations. Kim et al. (2001) studied the aerodynamic stability of fan rotor blades subjected to different forms of damage at 70% RPM. Reid and Urasek (1973) studied blades with localized damage to the leading edge due to external impacts and found that damage to the blade leading edge induced a decrease in the compressor aerodynamic performance, with a 3.5% decrease in efficiency compared to that of a compressor with undamaged blades. Tang et al. (2023) studied how the blade tip notch breakage influenced the aerodynamic traits for a transonic compressor rotor, finding that the blade began to display a near-stall state when the notch was deeper than 0.23 mm. Bohari and Sayma (2010) studied Rotor67 rotor blades, constructed blades with two different damage sizes to simulate bird-impact-damage blade deformation, and used a fluid dynamics method to analyze the aerodynamic trait change of fan at varying rotational velocities. Li et al. investigated the influence of blade tip damage over stability and surge margin of transonic compressor rotor blades through unsteady numerical simulations (Li & Sayma, 2012, 2015). Muir et al. addressed the aerodynamic problems of a turbofan engine fan during the takeoff phase of a bird strike (Muir & Friedmann, 2013, 2014, 2016). Jiang et al. (2017) explored how the local convex defects on blade surface affected the internal flow and aerodynamic behavior of a transonic compressor rotor. Li et al. (2018) found that impacted by external objects, the compressor blade leading edge produced blunt deformation, and that when the attack angle exceeded a certain scope, the blunt leading edge prominently changed the boundary layer evolution and affected the entire main-stream flow field. Liu et al. (2022) proposed a method for transforming bird-strike-deformed blades into aerodynamic models and subjected a compressor with deformed blades to the numerical aerodynamic simulations. Yang et al. (2021) selected a large-bypass-ratio fan from a certain civil aircraft for investigation, and they constructed three models with three different amounts of the blade missing above 50% of the blade height and a model with the whole piece completely missing for exploring the effect of fan aerodynamic behavior after a bird struck a fan blade. Through numerical simulations, Lu et al. investigated changes in the fan aerodynamic performance due to damage to a typical fan rotor blade caused by a medium bird, where experimental archive of a plane cascade was utilized (Lu, 2017; Lu et al. 2017). Qin et al. (2022) studied the characteristics and mechanism of the impact of tip drop block on the aerodynamic behavior of a transonic compressor rotor by numerical simulations. Yang (2014) established a geometric model of a fan with damaged blades based on the dynamic process of a bird strike and compared the aerodynamic property changes of fan before and following bird strike through numerical simulations. Cong et al. (2023) studied how the leading-edge tip damage affected the compressor aerodynamic traits.

In recent years, research around the world on damaged blades of compressors has mainly focused on the dynamic process of damage and structural design, while there have been fewer studies concerning how the blade damage affects the compressor aerodynamic performances. Because an aircraft cannot stop operating immediately when the compressor blade is damaged due to the engine's inhalation of foreign objects during flight, the engine still needs to operate with the damaged compressor rotor blade. Hence, it is profoundly meaningful to explore the effect of blade damage on the compressor aerodynamic performances and to reveal the mechanism underlying engine performance deterioration to ensure the aircraft flight safety.

In the present work, we investigated a low-speed axial compressor. Aerodynamic performance experiments and simulations of the original compressor and the compressor with damaged blades were carried out. The reliability of our numerical approach was experimentally validated. In addition, to study the rotor blade of the transonic compressor, damaged blades with different tip curling degrees were constructed, and the three-dimensional viscous numerical simulations were carried out. Through internal flow field comparison between the original compressor and that with damaged blades, the variation mechanism for compressor internal flow field alongside the influence of blade damage over the compressor aerodynamic properties were analyzed.

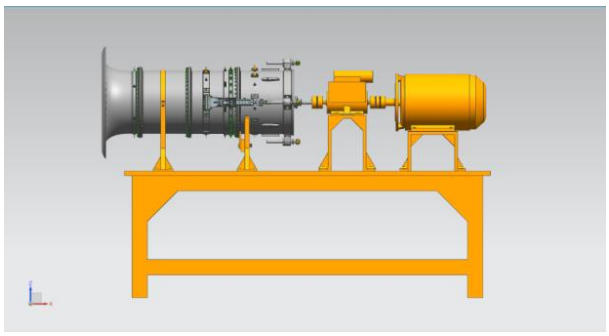

Fig. 1 Schematic diagram of low-speed compressor test bed

Table 1 Main design parameters of low-speed compressor

Design Parameters	Value
Rotational speed (r/min)	6000
Total pressure ratio	1.054
Flow rate (kg/s)	8.4
Outer diameter (mm)	400
Inner diameter of rotor/stator inlet (mm)	160/200
Number of rotor/stator blades	15/20

2. Experiment And Simulation Of Low-Speed Compressor

2.1 Experimental System

Figure 1 schematically illustrates the test bed for single-stage low-speed axial flow compressor. From left to right, the components include the bell mouth, outer compressor shell, rectifier cone, rotor blades, stator blades, inner compressor shell, supporting bracket, throttle, rotation shaft, speed torque sensor, as well as motor. Table 1 lists the major parameter settings for the investigated compressor (Charles et al., 1995; Boos et al., 1998).

To determine the aerodynamic parameters of the compressor, eight static pressure holes were evenly created circumferentially at the compressor rotor inlet and the compressor outlet, and the pressure sensor was connected to record the static pressure change of the wall surface. Moreover, eight five-point comb total pressure probes were uniformly distributed circumferentially at the compressor outlet, and the total pressure of outlet section was measured by arranging 40 points in total. Figure 2 schematically illustrates the five-hole total pressure probe and the layout diagram of aforementioned measuring points for the compressor outlet section.

Because parameters such as the geometric center of gravity of the damaged blade are different from those of the original blade, in order to better balance the whole row of blades, three drum-shaped damaged blades with a circumferential angle of 120° were used in the experiment, with which the damaged fan aerodynamic properties were determined. Figure 3 displays the physical diagram for the fan with damaged blades and the physical diagram of the arrangement of probe measuring points. During the

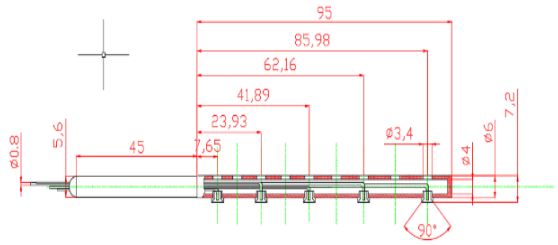

(a)

(b)

Fig. 2 Schematic diagram: (a) five-hole total pressure probe and (b) outlet total pressure measuring point layout

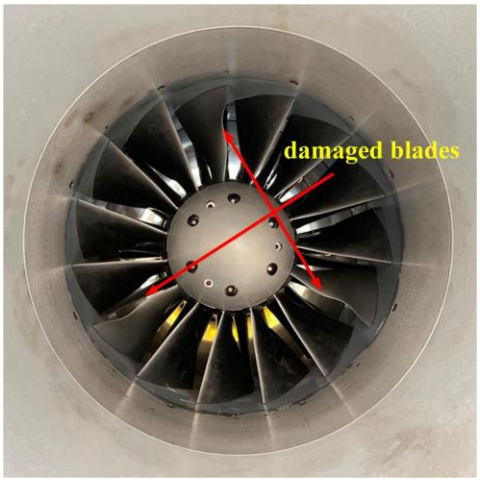

(a)

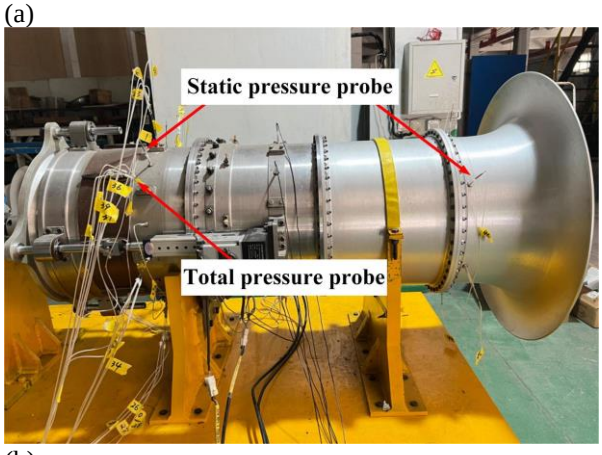

(b)

Fig. 3 Physical diagram: (a) fan with damaged blades and (b) probe arrangement

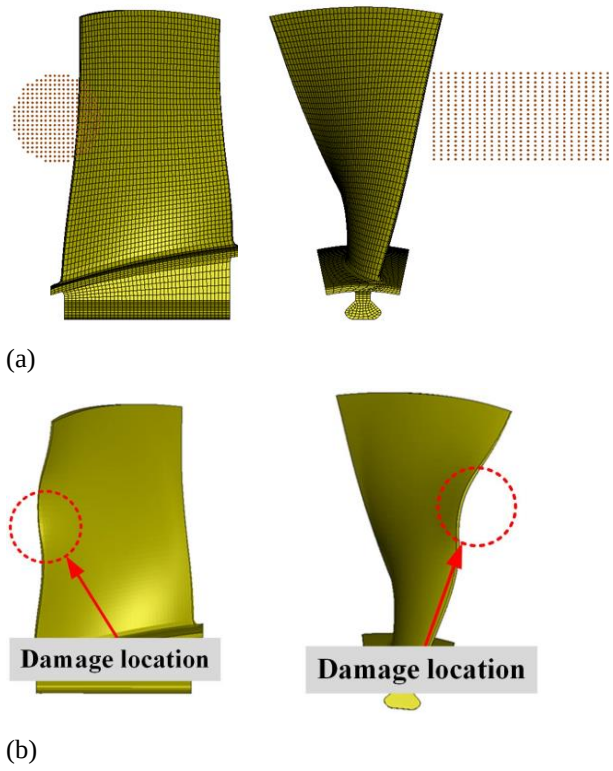

Fig. 4 Structure of low-speed damaged blade: (a) finite element model and (b) damage situation

measurement, the compressor working condition was first determined, and the corresponding throttle position was adjusted to change the back pressure and inlet flow rate. After the motor was started, the air flow was stable, and the atmospheric pressure along with temperature were measured. At the compressor outlet and inlet sections, the corresponding static pressure and total pressure were collected, and then the throttle opening was changed to continue the measurement for the next working condition.

2.2 Numerical Simulation Method

Before the aerodynamic property analysis and comparison between the prototype compressor and that with damaged blades, it was necessary to obtain a geometric model of the damaged blade. At present, there are two widely used methods (Barber et al., 1978): one is to carry out a bird impact experiment to create a damaged blade and use reverse engineering software to reconstruct geometric elements such as the feature lines and surface to establish a geometric model of the damaged blade; and the other is to use the FEM method for simulating the blade damage. Based on numerical simulation results, a damaged blade model that can perform flow field simulations is obtained.

Based on operation time and cost restrictions, the second method was adopted in this study. The following introduces the establishment of damaged blade model in the currently adopted model. Utilizing a gelatin cylinder whose compressibility is identical to that of a bird body mass density, we replicated the load produced by bird strike to impact blade 14. The blade was discretized into a hexahedral mesh, and the mesh size was 3 mm. The bird body was modeled with smoothed article hydrodynamics

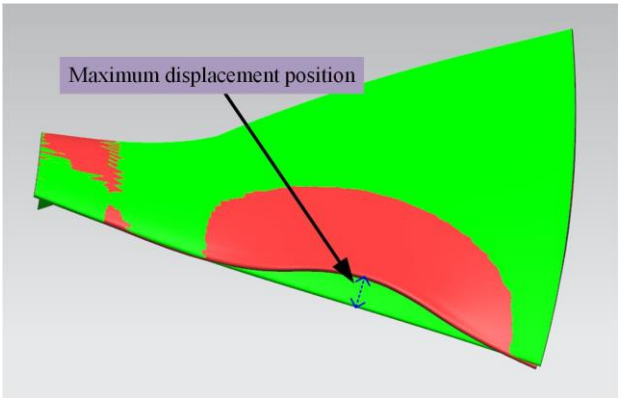

Fig. 5 Comparison of displacements between damaged and original blades

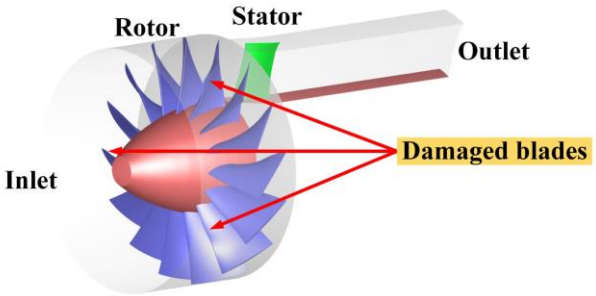

Fig. 6 Compressor simulation model with damaged blades

(SPH) particles. The blade had a 6000 r/min rotational velocity, while the bird was 100 g in weight. When the speed was 80 m/s, the middle portion of blade leading edge was impacted, and bird body particles contacted the blade by erosion contact. Figure 4 shows the FEM model for the blade alongside the damage after impact.

Figure 5 depicts the displacement contrast between the damaged and original blades. As is clear, although the blade did not break after completion of the impact, bulging was evident, and the largest deformation was located at approximately 65% of blade height. At this point, low-speed damaged blade model was established, which was utilized as a part of subsequent damaged blade in the full-channel numerical simulation model.

For the present aerodynamic simulations of compressors with damaged blades, a compressor model having three damaged blades evenly arranged in the circumferential direction every 120° was utilized, as shown in Fig. 6. In this study, the NUMECA AutoGrid5 module was used to construct the O4H structured grid for the simulation model. Grid independence verification was carried out for simulating the aerodynamic behavior of original compressor. Because the original compressor had an axisymmetric structure, the grid independence verification was carried out by single-channel simulations.

To obtain suitable y+ values along the blade surface, the first layer mesh thickness was selected as 0.007 mm. Reynolds-averaged Navier–Stokes (N-S) were employed as the governing equations, while the fourth-order Runge–Kutta was applied for obtaining an iterative solution. Spatial discretization was accomplished using the second-

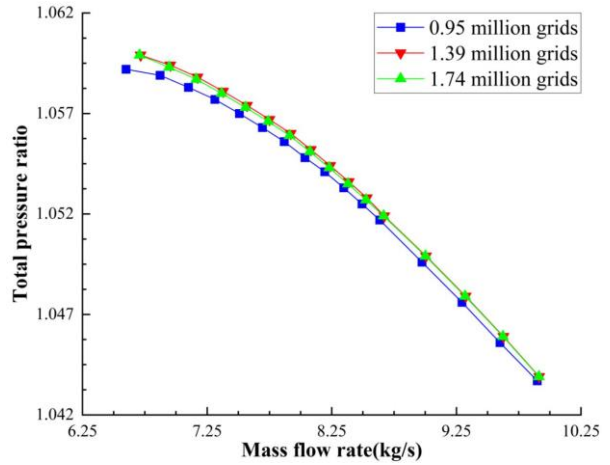

(a)

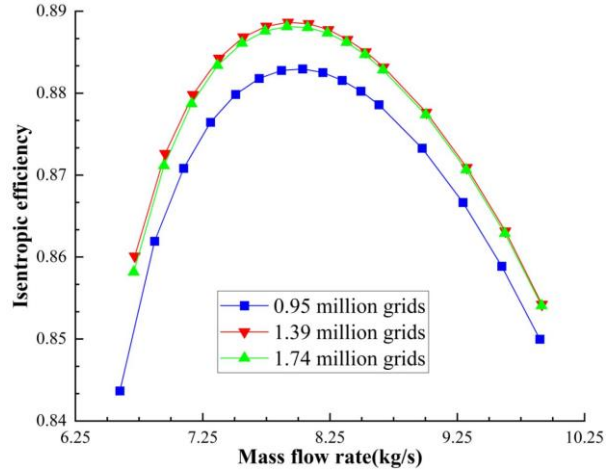

(b)

Fig. 7 Grid independence verification: (a) total pressure ratio–mass flow rate and (b) isentropic efficiency–mass flow rate

order precision central difference format, and the convergence was accelerated by the local time stepping and multi-grid techniques. Besides, the turbulence model adopted was Spalart–Allmaras (S-A). The boundary conditions of the simulation were as follows. The total inlet pressure was set as the standard atmospheric pressure, while the total temperature was adopted as the standard atmospheric temperature. Pressure boundary conditions at the axial inlet and outlet were radially uniform static pressures. In the simulation, the outlet pressure was gradually increased to approximate the compressor stall boundary, and the divergence point of simulations was used as the compressor stalling point.

In this study, three grids were investigated for grid independence verification, consisting of 0.95, 1.39, and 1.74 million elements. Figure 7 diagrammatizes the compressor aerodynamic performance characteristics calculated for different grids. As is clear, when the quantity of grid elements reached 1.39 million, its influence on the simulated compressor characteristics could be basically ignored. Therefore, the division scheme of a single-channel grid with 1.39 million elements was selected to generate a full-channel computational domain

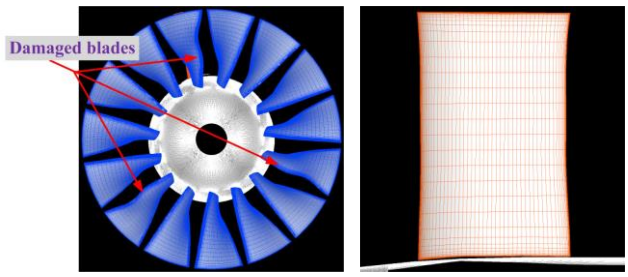

(a) (b)

Fig. 8 Blade surface grids for simulations: (a) rotor blade and (b) stator blade

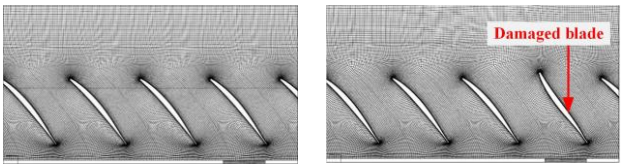

(a) (b)

Fig. 9 Grid comparison at 65% of the blade height B2B surface for simulations: (a) original rotor and (b) rotor with damaged blades

grid. Because the stator blade was undamaged and symmetric, the flow field details could be obtained by using a stator blade via a steady-state simulation. The quantity of grid elements in the whole computational domain was 11.79 million. Figure 8 depicts the computational grid for blade surface, whereas Fig. 9 displays the comparison regarding computational grids of the full-channel at 65% of the blade height B2B (blade to blade) surface for the original compressor and the compressor with damaged blades.

3. Numerical Simulation Of Aerodynamic Performance Of Transonic Compressor

3.1 Computational Model

To investigate how the blade damage affects the high-speed compressor performance, the Rotor37 blade designed by NASA was selected for this study. This rotor is used as the first-stage rotor in transonic compressors (Reid & Moore, 1978). In this study, the ring had 36 blades, the relative blade tip Mach number was 1.48, the design velocity and flow rate were separately 17188 r/min and 20.188 kg/s, and the isentropic efficiency was 0.877.

The performance parameters of the rotor were typical for transonic compressors. Detailed experimental data are available for this compressor, and thus, it was selected for analysis via numerical simulations. Figure 10 shows the full-channel simulation model of the Rotor37 rotor blade.

3.2 Simulation Method

To obtain damaged blades with different damage forms, the same construction method as that used for low-speed damaged blades was adopted. The Rotor37 blade

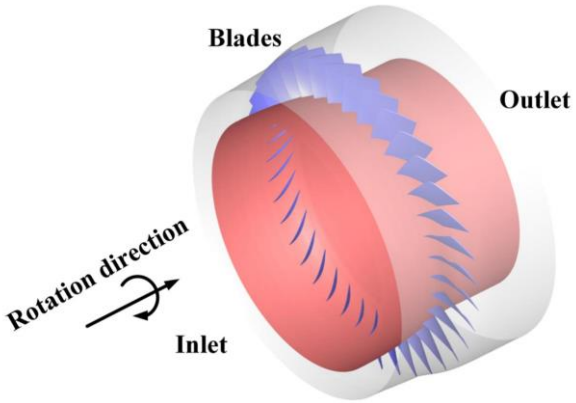

Fig. 10 Rotor37 rotor model diagram

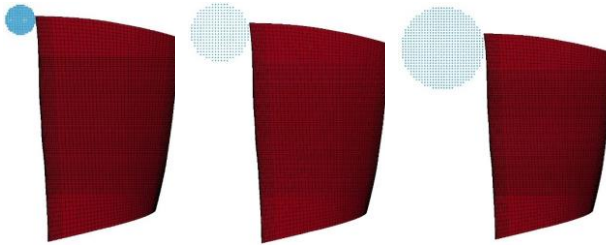

(a) (b) (c)

Fig. 11 FEM model for a bird striking the blade: (a) slight impact, (b) moderate impact, and (c) severe impact

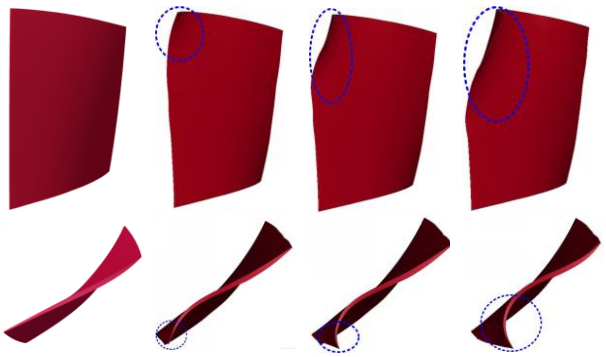

(a) (b) (c) (d)

Fig. 12 Rotor37 blades with different degrees of damage: (a) original blade, (b) slightly curled blade, (c) moderately curled blade, and (d) heavily curled blade

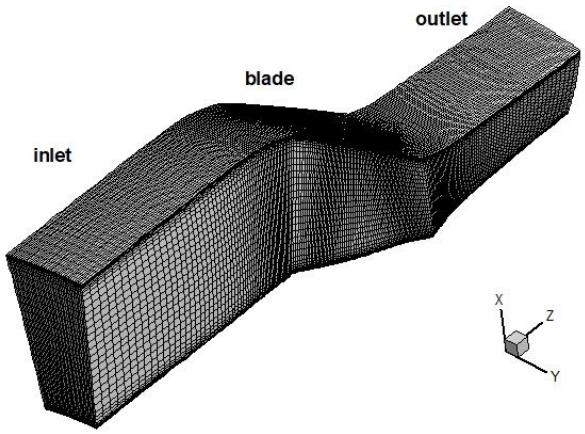

Fig. 13 Three-dimensional diagram of grid with 0.9 million elements for single-channel simulations

was discretized via a hexahedral grid 1.5 mm in size, and the grid of the blade leading edge was refined. Single-blade grid elements totaled 34400 in number. The blade was impacted by three kinds of bird bodies, while the bird body was modeled using SPH particles. The rotation constraint was set at the blade root, and the blade was impacted by bird at a 103 m/s velocity. Erosion contact was adopted between bird body particles and the blade. Fig. 11 illustrates the FEM model for a bird striking the blade.

Figure 12 depicts the damage resulting from three kinds of bird bodies striking the blade, and the circle shows the damage deformation position.

As is clear, the blade damage form was tip leading edge curling, and the blade did not tear. The curl degree of the blade leading edge intensified with the growing bird mass. At this point, the establishment of blade models with different damage degrees was completed, and these were subsequently used as the damaged blades in the full-channel numerical simulations.

The Rotor37 rotor was discretized with a structured grid using AutoGrid5. After curling of blade leading edge, the deformation at tip location caused the damaged blade to fail to maintain the same tip clearance as the original blade. Using AutoGrid5 to automatically quantify the same tip clearance could effectively avoid this problem. In the grid calibration, grid independence verification was also carried out by single-channel simulations of the original rotor. The numbers of grid elements for the three schemes for the single-channel simulations were 0.51, 0.9, and 1.56 million. Figure 13 shows a three-dimensional diagram of the grid with 0.9 million elements, and Fig. 14 shows the rotor characteristic curves under different grid numbers. To obtain suitable y+ values along the blade surface, the first-layer mesh height was selected as 0.003 mm. The inlet and outlet boundary conditions for the simulations were formulated using the same settings as those used for the low-speed compressor.

As revealed by the comparison of simulation outcomes with various grids, although the simulation results of these three grids were relatively consistent, the number of grid elements still had a certain influence on the results. As long as the quantity of grid elements exceeded 0.9 million, its influence on the simulated rotor characteristics could be ignored. Therefore, a 0.9 million grid element division scheme was used to mesh the full-channel computational domain. Mesh elements of the whole computational domain totaled 34.04 million in number.

To obtain the influence of blade curling degree over the compressor aerodynamic behavior, Rotor37 models having one slightly curled blade, one moderately curled blade, and one severely curled blade were established. For brevity, the original rotor and the damaged rotor models

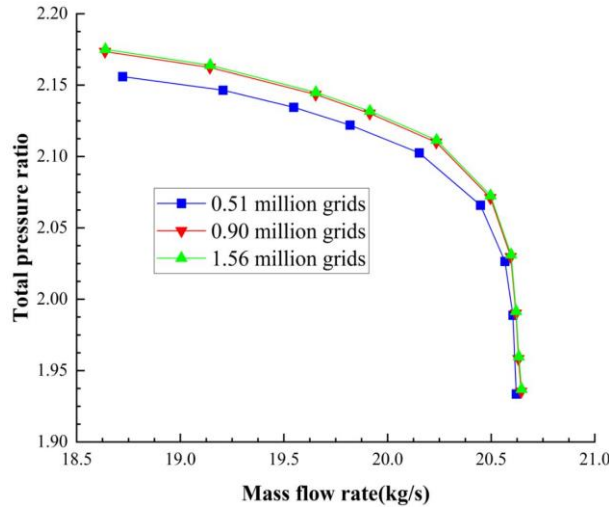

(a)

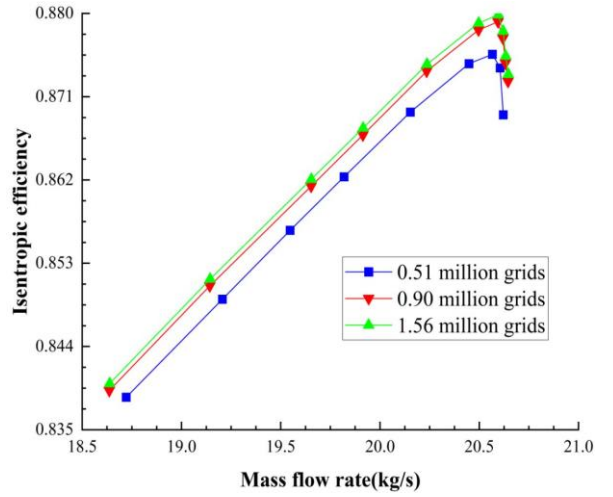

(b)

Fig. 14 Rotor37 rotor grid independence verification: (a) total pressure ratio–mass flow rate and (b) isentropic efficiency–mass flow rate

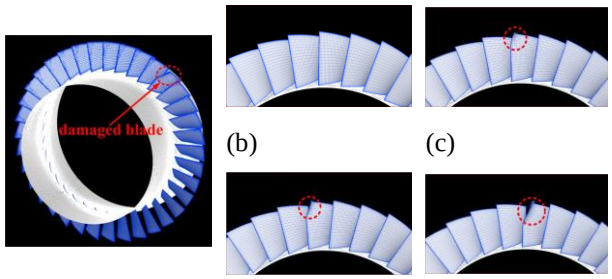

(a) (b) (c) (d) (e)

Fig. 15 Computational grids on the surface of each model blade: (a) full ring of D model, (b) local blades of A model, (c) local blades of B model, (d) local blades of C model, and (e) local blades of D model

with slightly, moderately, and severely curled blades were separately named models A, B, C, and D. Figure 15 depicts the surface grid for each model blade, and the circle in the figure shows the damaged blade.

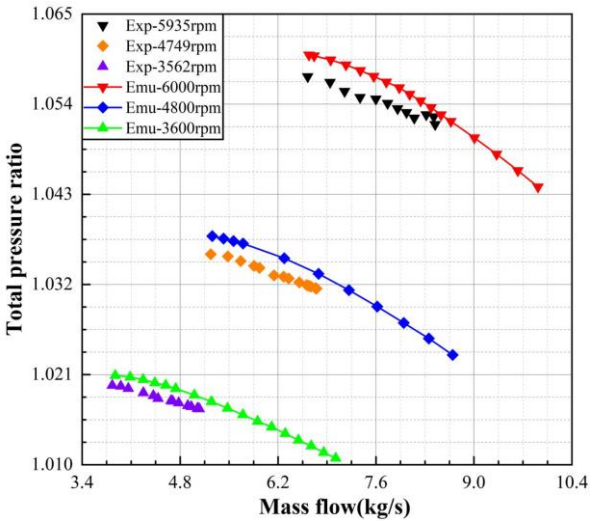

(a)

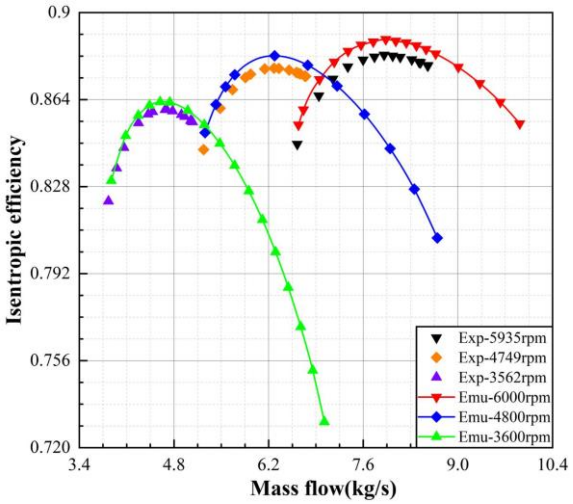

(b)

Fig. 16 Characteristics of the original low-speed compressor: (a) total pressure ratio–mass flow and (b) isentropic efficiency–mass flow

4. RESULT ANALYSIS OF LOW-SPEED COMPRESSOR

4.1 Comparison of Aerodynamic Characteristics Between Experiments and Simulations

Figure 16 compares experimental versus simulated characteristics for the original compressor at varying velocities, where all the experimental speeds are converted speeds. Since the opening of the valve was changed to achieve throttling in the experiment, the actual outlet static pressure could not be lower than atmospheric pressure, and the flow range of the compressor was limited. Therefore, the experimental data points had difficulty reaching a high flow state. As revealed by the comparisons of simulation and experimental outcomes in the diagram, the change characteristics of simulated efficiency and total pressure ratio coincided with those of the experiment, but the experimental values were generally lower. This was because the converted speeds

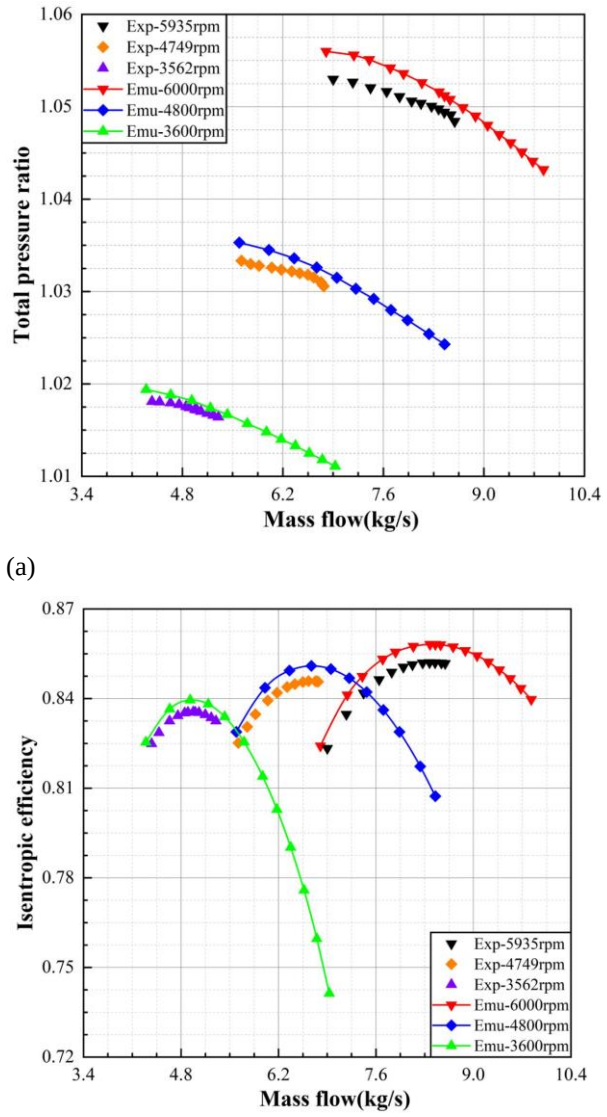

Fig. 17 Characteristics of low-speed compressor with damaged blades: (a) total pressure ratio–mass flow and (b) isentropic efficiency–mass flow

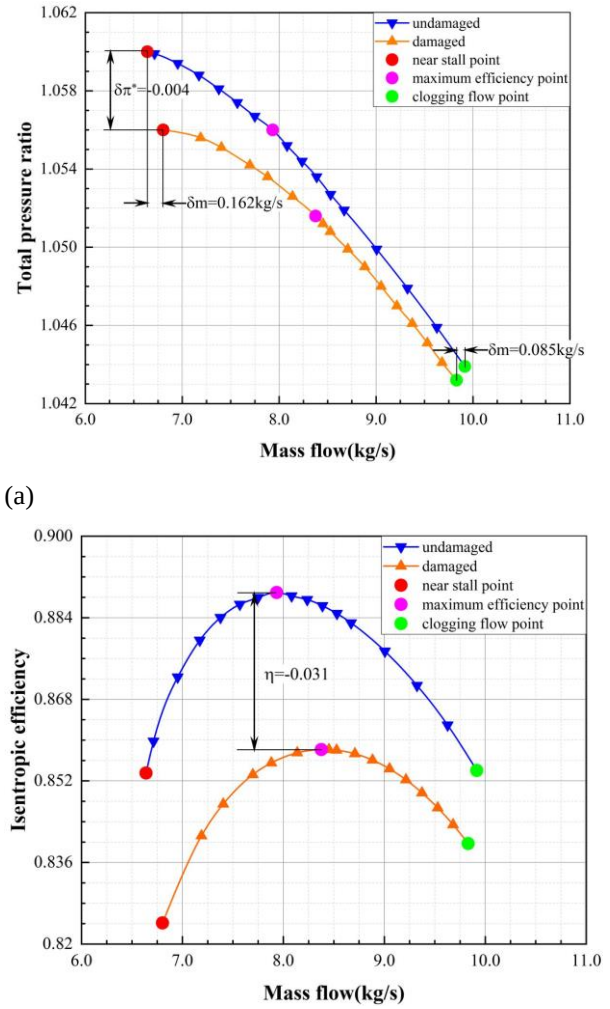

Fig. 18 Comparison of characteristics of low-speed compressor blades before and after damage (design speed): (a) total pressure ratio–mass flow and (b) isentropic efficiency–mass flow

were slightly lower than the simulated speeds at the physical speeds of the experiments. The simulation and experimental results at 100%, 80%, and 60% rotational speeds had maximum errors of the total pressure ratio of 0.59%, 0.39%, and 0.16%, respectively, and corresponding respective maximum errors of the efficiency of 0.65%, 0.51%, and 0.32%.

Figure 17 illustrates the comparison of experimental versus simulation characteristics for a compressor with three bulging blades at varying speeds. As is clear, after the blade was damaged, the experimental and simulation characteristics of the compressor were still consistent. Within the range of the rotational speed error, the simulated values somewhat exceeded the experimental values. Calculated and experimental results at 100%, 80%, and 60% rotational speeds were obtained at identical flow rate. Maximum errors of the total pressure ratio were 0.29%, 0.18%, and 0.08% respectively, and the corresponding maximum errors of the efficiency were 0.61%, 0.52%, and 0.40%, respectively. The comparison unravels that the experimental findings were highly close to the simulation outcomes within the permissible error range. Our proposed numerical simulation approach could capture the variation characteristics of the compressor aerodynamic performance, thus verifying its feasibility.

To compare the influence of blade damage over the compressor behavior at design speed, the characteristics comparison between the original compressor and that with damaged blades is presented in Fig. 18. The design point shown in Table 1 was the design condition, and the stability margin formula is:

$$SM = \frac{\left(\pi^* / \dot{m}\right)_s - \left(\pi^* / \dot{m}\right)_d}{\left(\pi^* / \dot{m}\right)_d} \tag{1}$$

where SM is the stability margin, π^* signifies total pressure ratio, $\dot{m}$ signifies flow rate, subscript s represents the near-instability condition, and subscript d stands for design condition (assuming that the original design state is the design point parameter after damage).

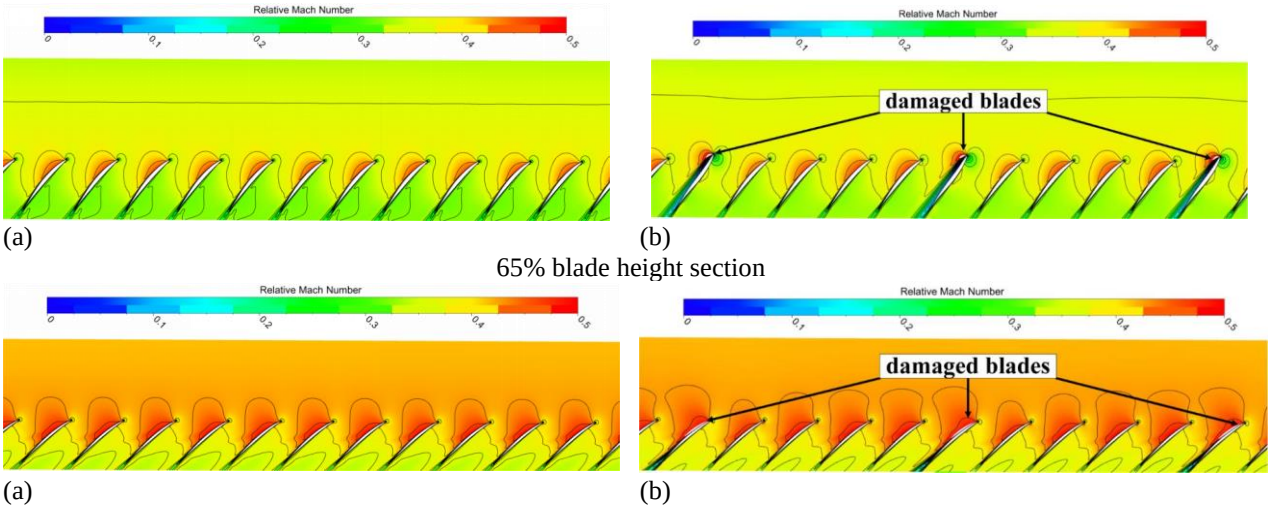

Fig. 19 Comparison of relative Mach number contours of different blade height sections (clogging condition): (a) original rotor and (b) damaged rotor

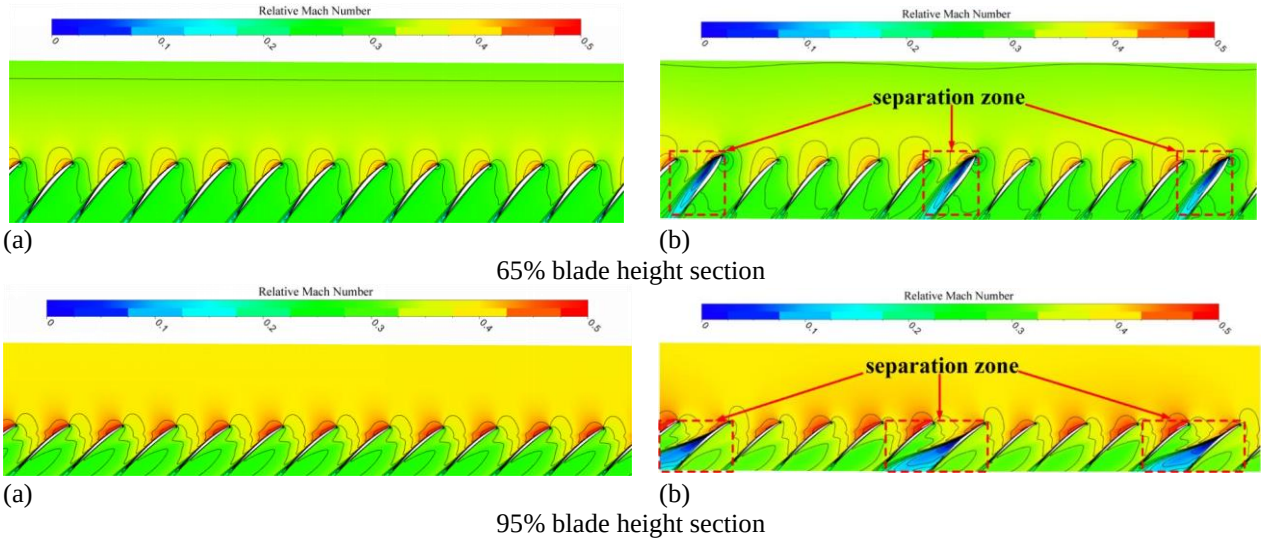

Fig. 20 Comparison of relative Mach number contours of different blade height sections (maximum-efficiency condition): (a) original rotor and (b) damaged rotor

Stability margin was 27.07% for the original compressor, whereas was 23.65% for the damaged compressor. Thus, the stability margin was reduced by 3.42% by the damage. According to Fig. 18, the compressor characteristic graphs with the damaged blades shifted down overall, and the aerodynamic performance decreased significantly. The flow rate at the clogging point was relatively reduced by 0.86% compared to that without damage, the flow rate near stall point grew by 2.44%, the stable working flow boundary range was reduced by 7.56%, and the maximum efficiency was reduced by 3.1%. To better analyze the causes of compromise in compressor aerodynamic properties, we analyzed the flow fields for the three typical operating points in Fig. 18.

4.2 Flow Field Analysis of Clogging and Maximum-Efficiency Conditions

To comprehend the causes of deteriorated aerodynamic properties for the compressor rotor under the clogging and maximum-efficiency conditions, Figs. 19 and 20 show the relative Mach number contours for various blade height sections of the original compressor rotor and the rotor with damaged blades under these two conditions. In case the efficiency is maximum, the flow of the rotor with bulging blade in the middle and tip sections was significantly different from that of the original rotor. The main performance characteristics were as follows. A low-speed zone was present on the bulging blade suction side. The low-speed region in the blade middle section extended from leading to trailing edge of damaged blade, occupying about 25% of circumferential range of the damaged blade channel. This was because after the blade was damaged, the section had the same height as the blade with the largest damage deformation, and its geometric inlet angle increased significantly. This resulted in an attack angle enlargement of incoming flow, causing boundary layer separation of the damaged blade suction surface, resulting in a broad scope of low-speed zones. This phenomenon was not evident under the blocking condition, which was due to the lower outlet back pressure in such context, as well as the larger Mach number in main-stream region and the smaller boundary layer separation area on the damaged blade suction surface.

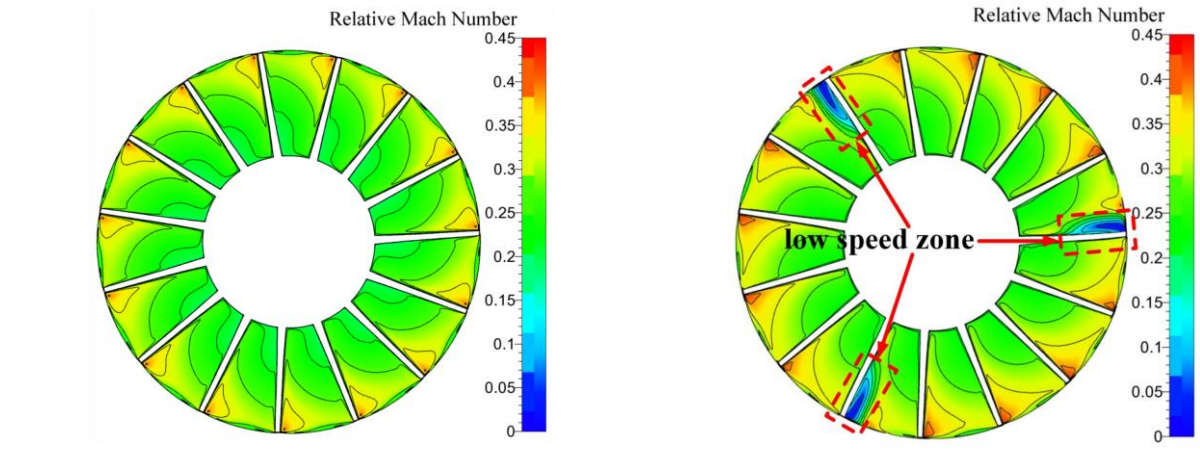

(a) (b)

Fig. 21 Comparison of relative Mach number contours of axial 50% chord length section (maximum-efficiency condition): (a) original rotor and (b) damaged rotor

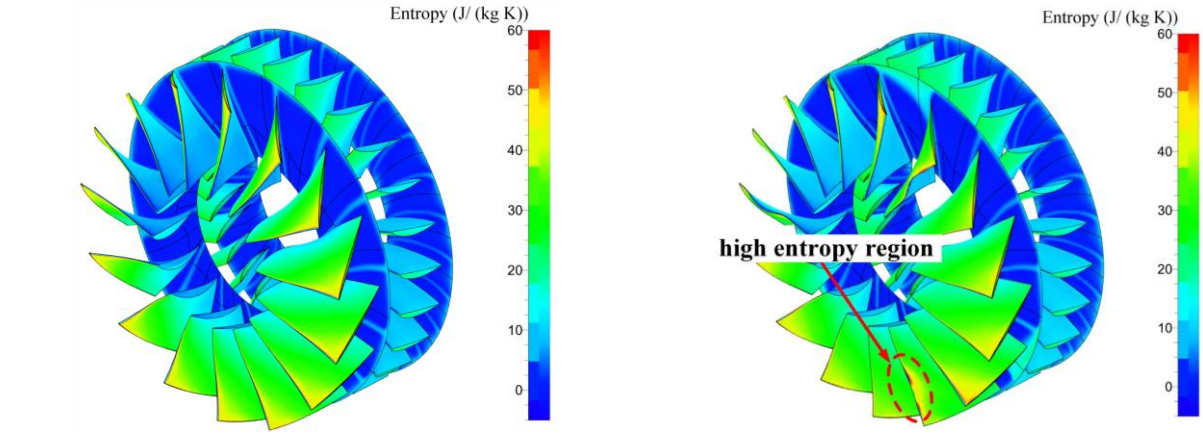

(a) (b)

Fig. 22 Comparison of entropy contours of whole flow field (maximum-efficiency condition): (a) original rotor and (b) damaged rotor

Under the maximum-efficiency condition, the blade shape change of the blade tip section was not as severe as that of the 65% blade height, but it led to an attack angle enlargement for incoming flow. Therefore, the low-speed region only started from 40% chord length of the damaged blade suction surface and extended downstream. Nonetheless, because the flow separation of the tip section was doped with coupling of the tip clearance flow, the circumferential range of influence as the low-speed zone developed downstream was gradually expanded, and the whole circumferential range of the suction-side channel for the damaged blade was occupied as the flow moved to its trailing edge.

Figure 21 illustrates the relative Mach number contour comparison for 50% axial chord length section between the original and damaged rotors in the maximum-efficiency state. Clearly, the low-speed region on the damaged blade surface occupied partial channel area, which extended from the blade bulge position to tip, although failing to affect the flow of neighboring channels following the flow squeezing through main-stream area in the channel. Moreover, the relative Mach number gradient on the blade surface seldom changed in this condition, and large flow separation was absent. This was also the primary reason that the compressor could still operate stably under this condition.

Figure 22 depicts the entropy contours for the whole compressor flow field in the maximum-efficiency state. Clearly, an evident high-entropy area was present in the leading edge vicinity of damaged blade surface, which expanded to the blade tip along the span direction, showing consistency with the low-speed region of the damaged blade suction surface. This indicated that the boundary layer flow separation led to the emergence of a low-speed and high-entropy area, which also increased the flow loss and caused compromise in the compressor aerodynamic properties.

Figure 23 displays the static pressure distributions on blade surface for the original and damaged blades at various blade height sections under the maximum-efficiency condition. At the 65% blade height section, the suction surface static pressure at the blade leading edge was higher for the damaged blade than for the original

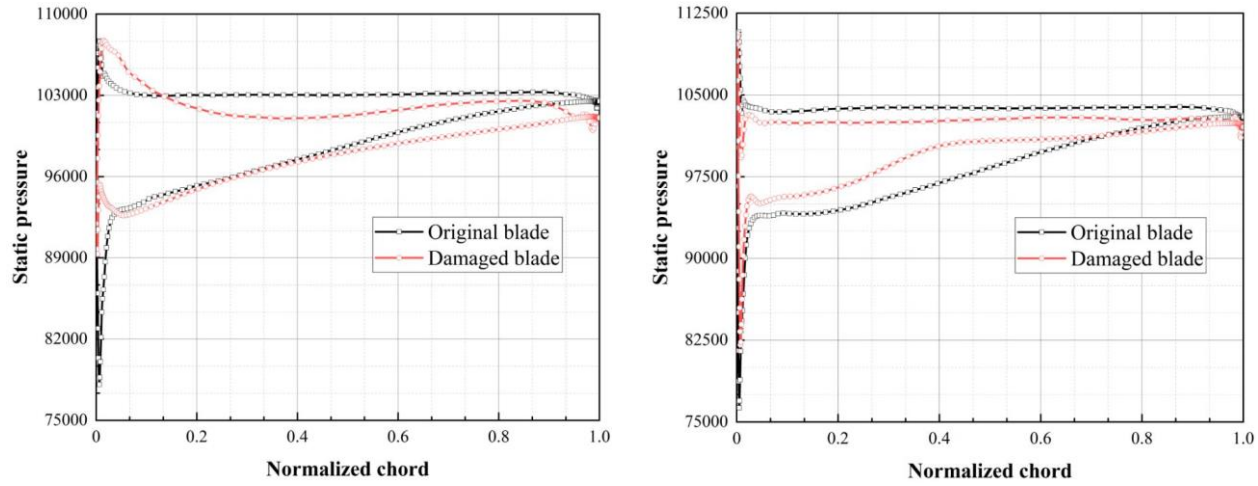

(a) (b)

Fig. 23 Static pressure distributions on the blade surface of different blade height sections (maximum-efficiency condition): (a) 65% blade height section and (b) 95% blade height section

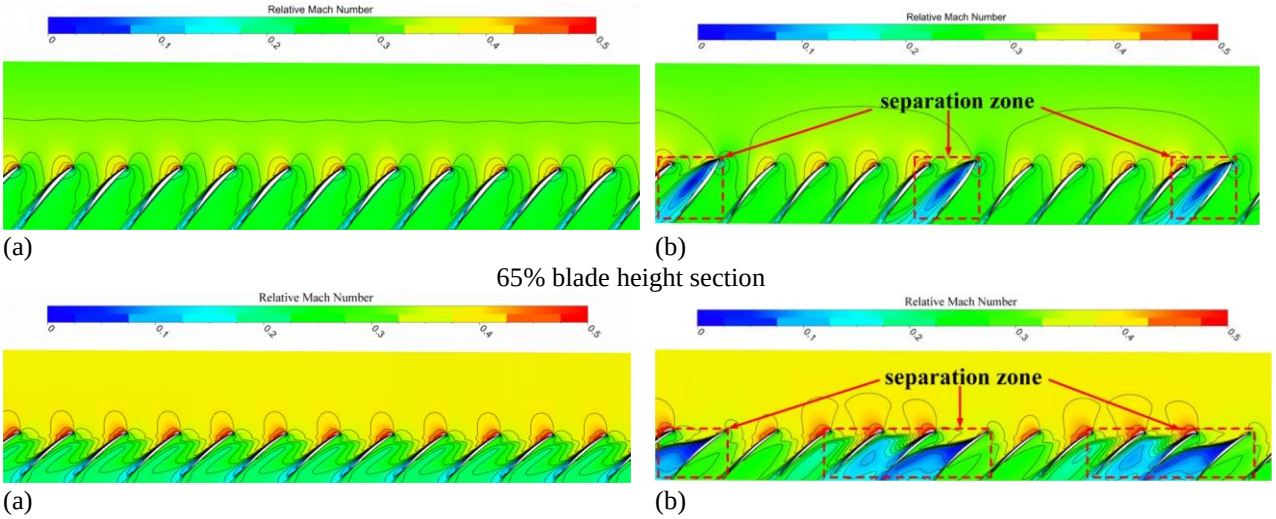

(a) (b)

65% blade height section

(a) (b)

95% blade height section

Fig. 24 Comparison of relative Mach number contours of different blade height sections (near-stall condition): (a) original rotor and (b) damaged rotor

blade. At the 95% blade height section, the maximum static pressure difference on the suction surface between these two blade types was near 40% of the chord length, showing complete coincidence with the starting position of low-Mach-number zone in the different blade height sections of the damaged blade. Additionally, before 10% of the chord length in the damaged blade middle section, the blade surface pressure difference increased rapidly, leading to an rise in the inverse pressure gradient, and the boundary layer separated beforehand, which aggravated the degree of flow loss and led to a decline in performance.

4.3 Flow Field Analysis of Near-Stall Condition

Figure 24 displays the relative Mach number contour comparisons for different blade height sections under the near-stall condition. In contrast to the first two conditions, the flow decelerated because of the continuous increase in the outlet back pressure, the attack angle of incoming flow further increased, and the pressure gradient at blade leading edge decreased. The boundary layer could merely resist a limited inverse pressure gradient, and separation of flow occurred at the blade rear. In the case of damaged rotor, the flow separation on the blade surface produced a large scope of low-speed zones in the downstream neighboring channels along the rotation direction, thus intensifying the flow channel obstruction.

Moreover, flows in each blade channel of the original rotor were basically identical, and separation of flow occurred on the suction side of channel middle, which expanded downstream to result in stall of the entire compressor. For the rotor with damaged blades, there were a few low-speed regions on the damaged blade surfaces. Upon the blade channel blockage by low-speed region, the inlet flow angle of succeeding blade channel enlarged in the rotor rotation direction, making it the next stall channel. Accordingly, the compressor exhibited performance reduction and entered a stall state beforehand, which was also the reason for the advanced surge point of compressor characteristic curve following the blade damage.

Figure 25 shows the relative Mach number contour comparisons for the axial 50% chord section in the near-stall state. In contrast to the maximum-efficiency state, the

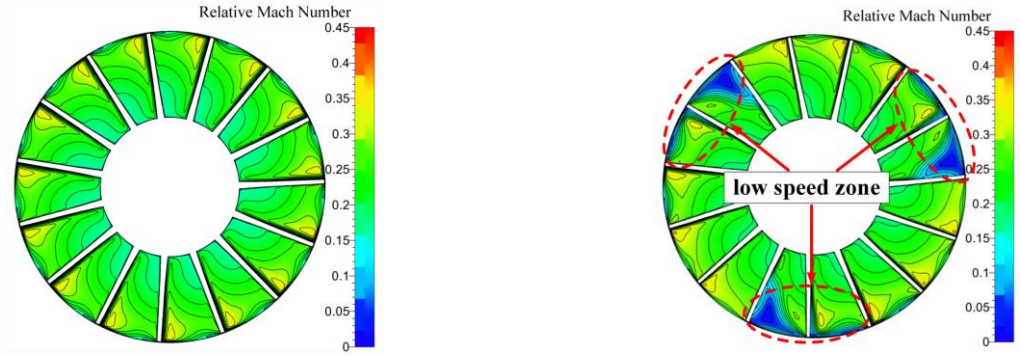

(a) (b)

Fig. 25 Comparison of relative Mach number contours of axial 50% chord length section (maximum-efficiency condition): (a) original rotor and (b) damaged rotor

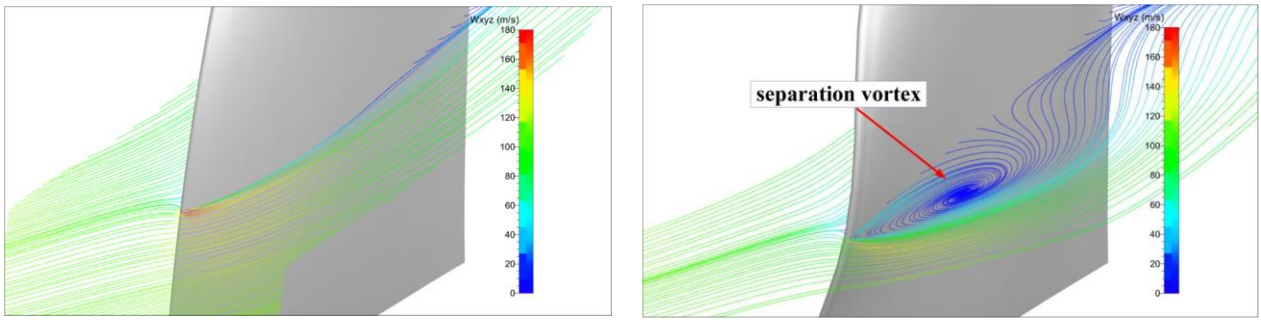

(a) (b)

Fig. 26 Streamline comparison of the original blade and the bulged blade at 65% blade height section: (a) original blade and (b) damaged blade

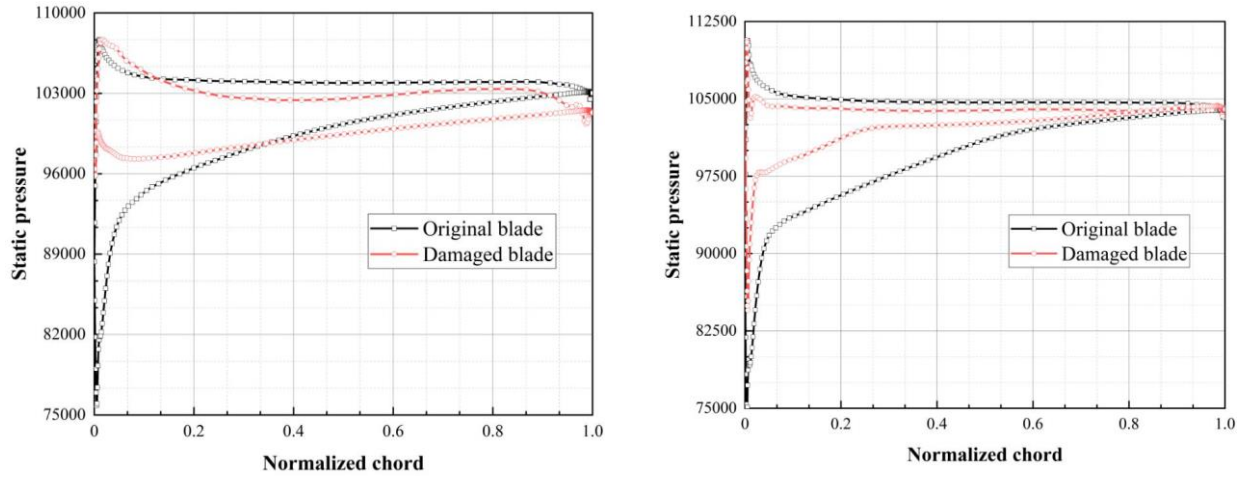

(a) (b)

Fig. 27 Static pressure distributions on the blade surface of different blade height sections (near-stall condition): (a) 65% blade height section and (b) 95% blade height section.

circumferential scope covered by low-speed region in the blade channel comprising damaged blades progressively expanded, influencing the neighboring channels in the rotation direction. The circumferential scope covered by low-speed region near the tip clearance reached six channels. In case the back pressure continued to increase, the circumferential scope would expand ongoingly, which would significantly reduce the compressor aerodynamic properties, ultimately leading to stability boundary crossing and stalling.

Figure 26 shows the streamline comparison between the original and damaged blades at the 65% blade height section under this condition. Clearly, in contrast to the original blade, the damaged blade deformed near the leading edge, resulting in a large amount of backflow gas on the blade suction side. These low-energy fluids and backflow gases formed a significant separation vortex structure along the blade. The separation vortex at 35% of the blade chord length had a distinct vortex core configuration. The significant chord flow separation vortex structure caused a sharp reduction in the compressor outlet flow within the blade height scope, and the flow loss increased.

Figure 27 displays the static pressure distributions on blade surface for various blade height sections in the near-stall state. In contrast to the maximum-efficiency state, it

Table 2 Comparison of aerodynamic parameters of different models

Parameter Variation	Model B	Model C	Model D
Clogging point flow rate	−0.24%	−1.36%	−2.79%
Near-stall point flow rate	+3.66%	+4.83%	+5.89%
Stable working flow boundary range	−35.36%	−58.16%	−83.03%
Near-stall point total pressure ratio	−3.03%	−5.32%	−10.02%
Maximum efficiency	−0.42%	−1.48%	−2.50%
Stability margin	−8.43%	−11.56%	−17.25%

Note: "+" means increase, "−" means decrease.

can be found that as the throttling continued, the blade surface static pressure increased, while the distribution trend along the chord direction basically did not change. However, pressure difference on the damaged blade surface in the tip section gradually decreased, which meant that the mechanical energy conversion efficiency of the blade decreased, resulting in a poor compression effect and overall performance degradation, which was consistent with the efficiency and total pressure ratio results for the compressor after damage.

5. Analysis Of Simulation Results Of Transonic Compressor Rotor

5.1 Aerodynamic Characteristics Analysis

Figure 28 depicts the aerodynamic performance comparison for the model rotor having different curled blades at the design speed, where the black dots represent experimental values of the Rotor37 rotor reported previously (Suder, 1996). After the blade was damaged, the efficiency along with total pressure ratio for each model rotor decreased significantly under all stable working conditions, and the aerodynamic performance decreased more sharply as the blade curl intensified. Besides, compared to the stable operating flow state of original rotor, as the curling degree increased, the flow rate at rotor clogging point gradually decreased, the flow rate near the stall point gradually increased, the stable rotor operating range became increasingly smaller, and the maximum efficiency point gradually shifted to the left. Table 2 shows the changes of the aerodynamic parameters of each model rotor compared with those of the original rotor.

The pre-damage rotor characteristics obtained by simulations resembled the experimental findings, and the maximum error of aerodynamic parameters at the same flow rate and boundary point was not more than ±5%. The further step showed the feasibility of the presently proposed numerical simulation approach. As revealed by the comparison of simulated rotor aerodynamic traits prior to and following the damage, the aerodynamic performance of damaged rotor was different from that of the undamaged rotor, but the variations of the characteristics prior to and following the damage were consistent, suggesting that the numerical outcomes could reflect the overall characteristics of the damaged blade effect on the compressor rotor aerodynamic properties reasonably. Hence, the numerical simulation approach used in the present work for the damaged blade is reasonable.

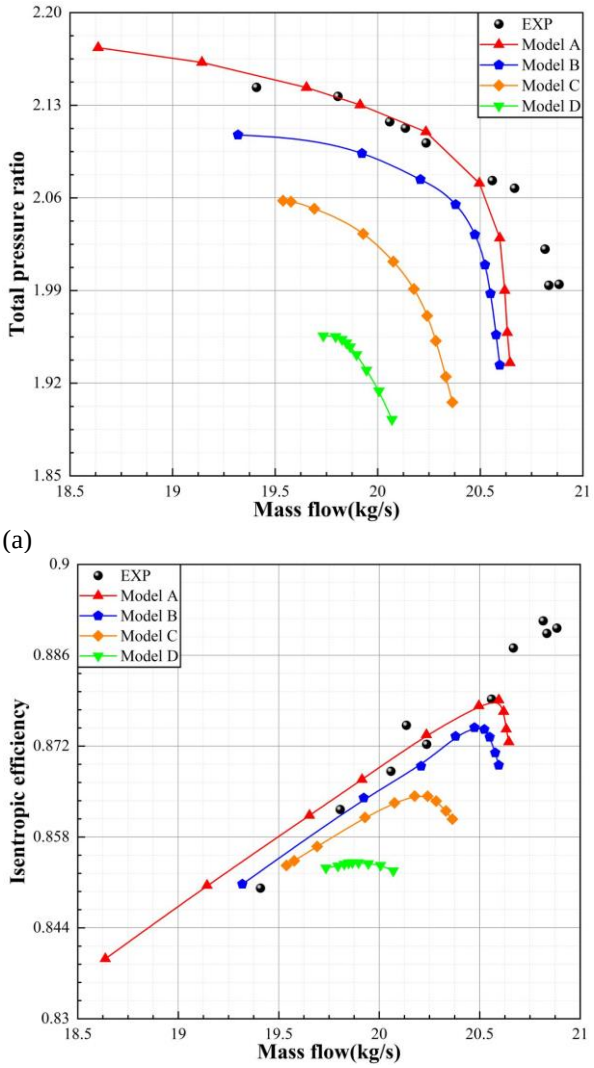

Fig. 28 Aerodynamic performance comparison of Rotor37 rotor before and after curling: (a) total pressure ratio–mass flow and (b) isentropic efficiency–mass flow

To evaluate the compressor performance following blade damage in more detail, the total pressure rise coefficient and loss coefficient were used as indicators (Zhang et al. 2015). The former coefficient is formulated as

$$\Phi_{tt} = \left(P_2^* - P_1^*\right) / \left(0.5\rho U_m^2\right), \tag{2}$$

where P_1^* and P_2^* separately signify the mean absolute total pressure values for rotor inlet and outlet, ρ signifies

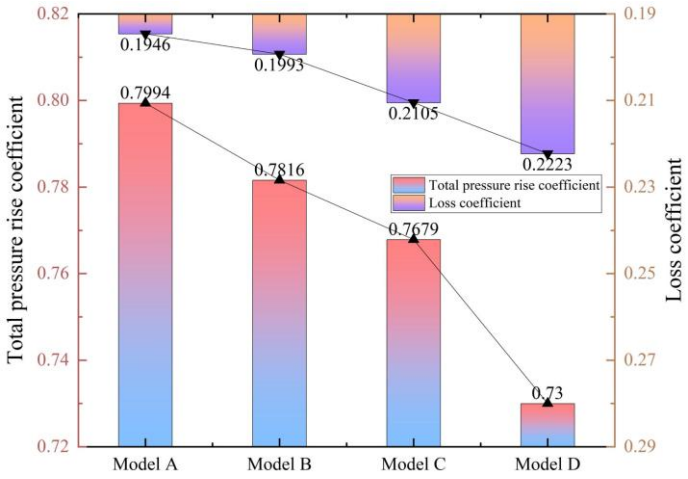

Fig. 29 Performance comparison of peak efficiency points of each model

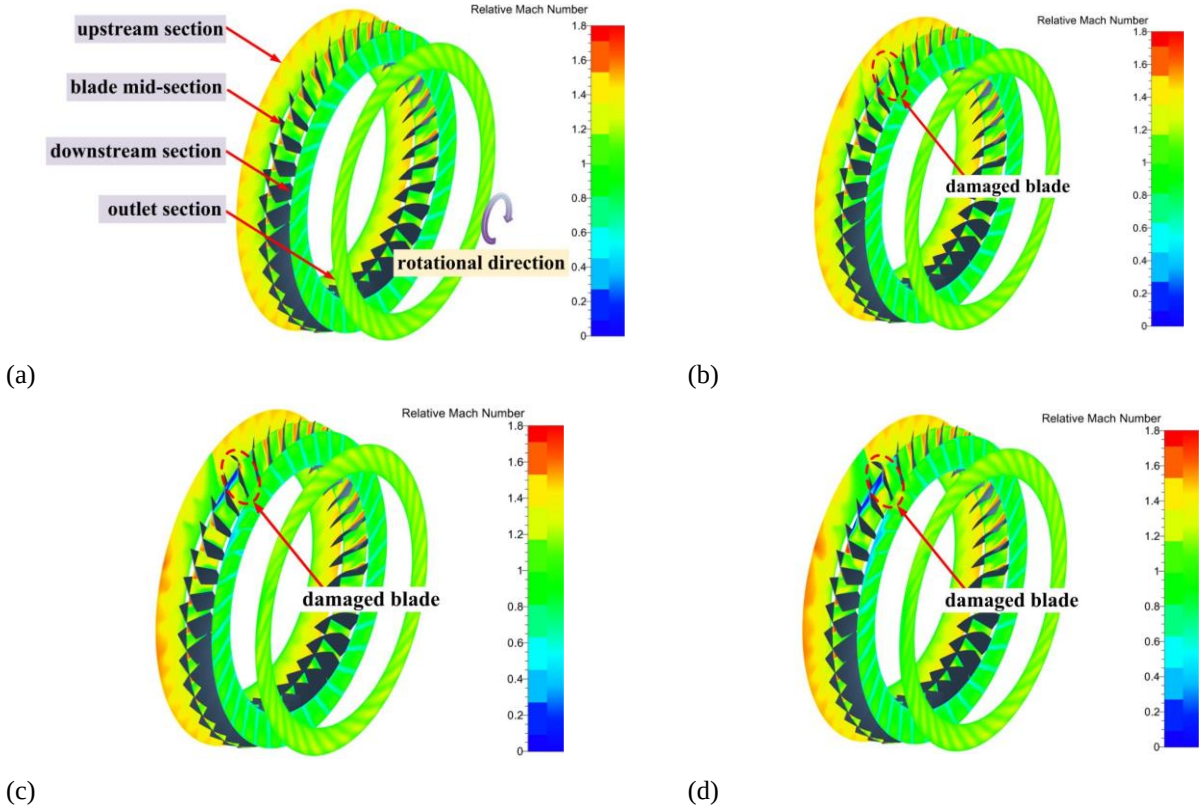

Fig. 30 Comparison of relative Mach number contours of different axial sections of each model (clogging condition): (a) model A, (b) model B, (c) model C, and (d) model D.

inlet density, and U_m signifies rim speed. The loss coefficient is defined as

$$\overline{\omega} = \left(P_{1w}^* - P_{2w}^*\right) / \left(P_{1w}^* - P_1\right), \tag{3}$$

where P_{1w}^* and P_{2w}^* separately signify the mean relative total pressure values of the rotor inlet and outlet, and P_1 denotes the mean static pressure at the inlet.

Figure 29 illustrates the comparisons of total pressure rise and loss coefficients for each model rotor at the peak efficiency point. From the figure, it is clear that as the degree of curl of the damaged blade gradually increased, the former coefficient gradually decreased, and the latter coefficient gradually increased. This showed that after the blade curled, the working ability of the compressor rotor decreased, and the flow loss also increased. Furthermore, the effect became more significant with the increase in the degree of damage.

5.2 Flow Field Analysis of Different Damage Degree Models Under Clogging and Maximum-Efficiency Conditions

To clarify the causes of aerodynamic property compromise with the damaged rotor near the clogging and maximum-efficiency conditions, Figs. 30 and 31 show the relative Mach number contours for various axial sections

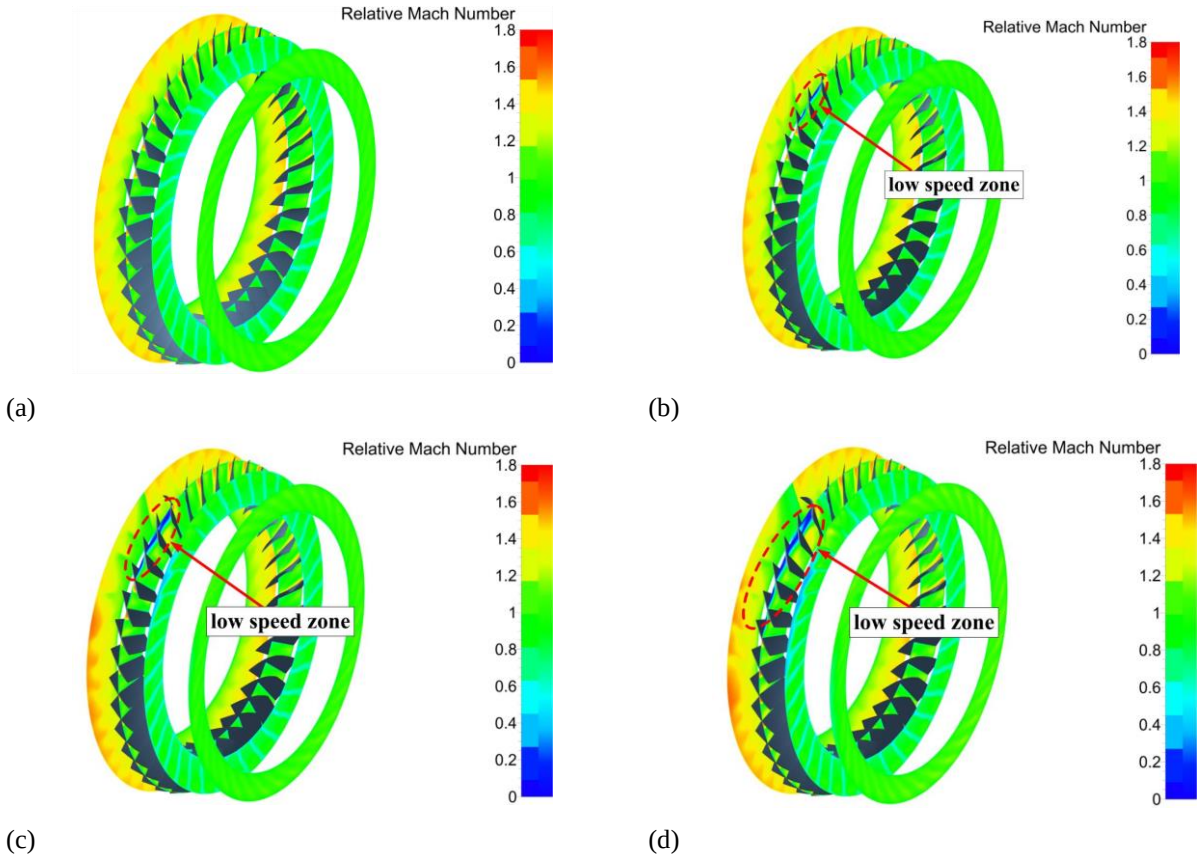

Fig. 31 Comparison of relative Mach number contours of different axial sections of each model (maximum-efficiency condition): (a) model A, (b) model B, (c) model C, and (d) model D

of rotor under the two conditions. According to these figures, the flow field structure of damaged rotor was relatively consistent in the area far from the damaged blade, and the circumferential inhomogeneity was not significant. However, the flow field structure in damaged blade area was significantly different, which was mainly manifested in the large-scale low-speed region in the damaged blade channel and its adjacent channels in the reverse rotation direction. With the increase in the curling degree, the low-speed zone occupied more channels. The low-speed region was located at the channel top, mainly concentrated in the channel formed by the damaged blade suction surface alongside the neighboring blade pressure surface. This was because after the blade was curled, the inlet angle of blade shape at the corresponding radial position increased significantly, leading to an attack angle enlargement of airflow, causing boundary layer separation along the damaged blade as well as the blade channel clogging, thereby resulting in the flow capacity reduction of the entire rotor. Given the rise of back pressure, the attack angle of incoming flow increased. Thus, this phenomenon was more evident under the maximum-efficiency condition compared with the clogging condition.

Figure 32 depicts the relative Mach number contours for various blade height sections. Since the blade shape change caused by blade damage was mainly concentrated in the tip area, there were no evident low-speed areas in the blade middle and root sections. At the 95% blade height section, a large scope of low-speed zones appeared in the blade channel on the damaged blade suction side. These zones started from the blade leading edge and covered the downstream area, almost covering the entire blade passage, which was also caused by the boundary layer separation. It was transmitted in the reverse rotation direction. As the degree of blade damage increased, the low-speed zone gradually expanded. When the blade was slightly, moderately, and severely curled, the numbers of blade channels covered by the low-speed zone were 2, 3, and 5, respectively. At this blade height, the detached shock wave generated at the damaged blade leading edge was stronger, the Mach number reduction after the wave was more evident, and the range of influence was larger. The channel shock wave in the channel covered by the low-speed region was pushed to the upstream area near the inlet of the blade channel. A local high-speed region appeared in the upstream area of the blade channel on the left side of low-speed zone. This was attributable to the combined effect of the blockage of adjacent channels and the disappearance of the influence of the extended shock wave of the damaged blade, resulting in a sharp rise of inflow Mach number to generate a local high-speed region.

Figure 33 shows the comparison of the three-dimensional tip clearance leakage flow lines of each model. In contrast to the original blade, the tip clearance flow of tip-rolled blade showed a more complex phenomenon. As the blade tip curling intensified, the air flow that originally impacted the blade tip suction surface could not directly flow into the channel, which led to the

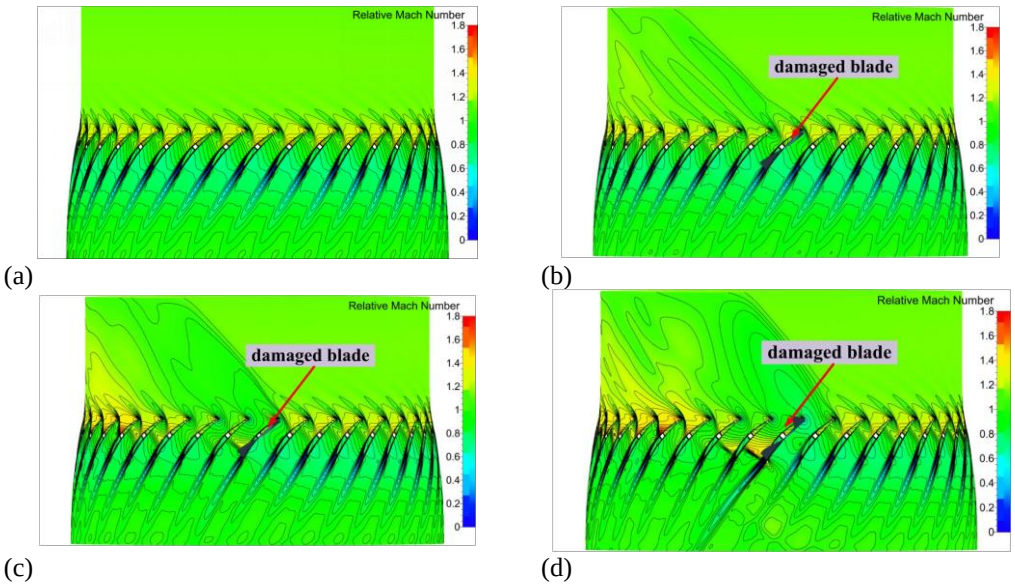

Fig. 32 Comparison of relative Mach number contours of different blade height sections of each model (maximum-efficiency condition): (a) model A, (b) model B, (c) model C, and (d) model D

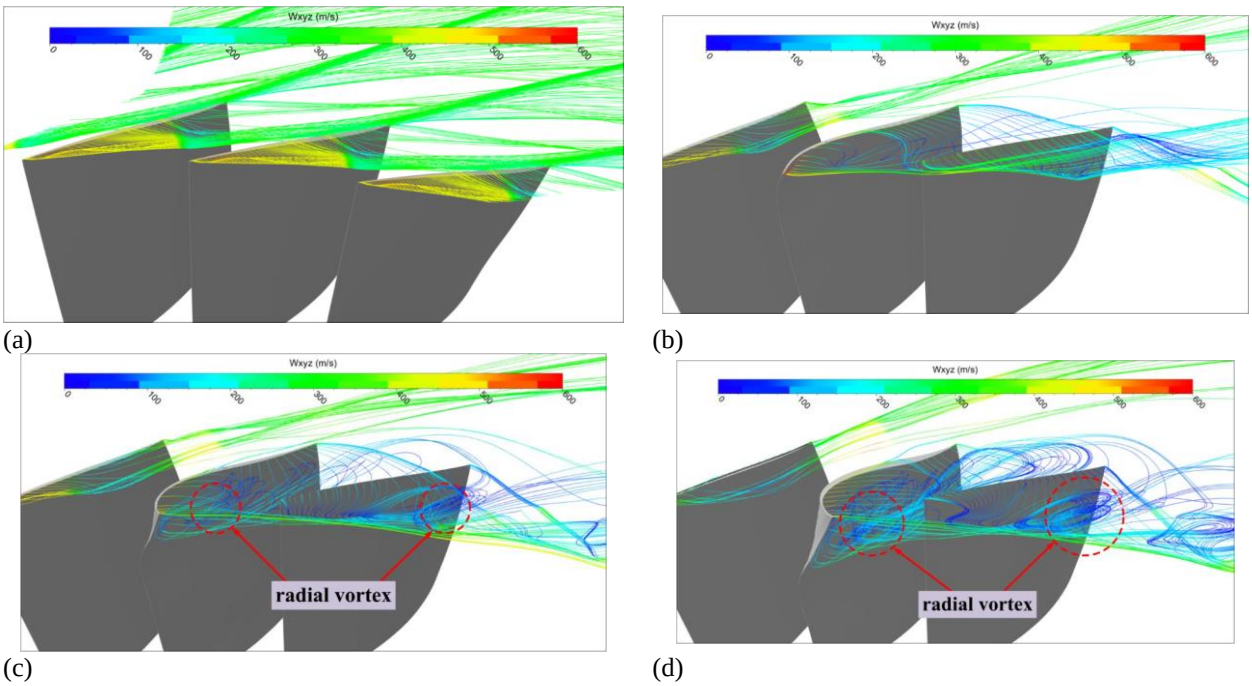

Fig. 33 Comparison of three-dimensional tip clearance leakage streamlines of each model: (a) model A, (b) model B, (c) model C, and (d) model D

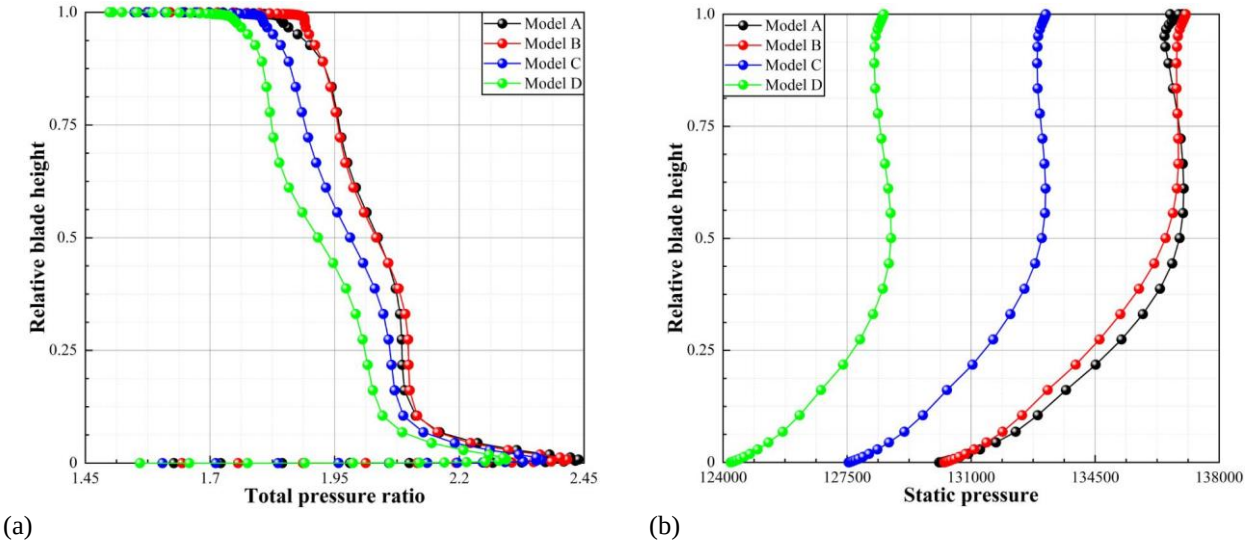

Fig. 34 Rotor outlet parameter distributions along the radial direction (maximum-efficiency condition): (a) total pressure ratio and (b) static pressure

secondary flow enhancement in the damaged blade tip clearance as well as a radial vortex formation under the high-speed centrifugal force of the compressor (indicated by red dotted circle in the figure). Moreover, this vortex flow also affected the tip clearance flow of the adjacent blades (counter-rotating direction) of the damaged blade, which gradually expanded the circumferential range of the radial vortex, resulting in blockage of the flow channel and significantly deteriorating the performance of the rotor.

Figure 34 illustrates the static pressure and total pressure ratio distributions along the blade height at the rotor outlet. As is clear, after the blade was curled, the two rotor outlet parameters decreased over the whole blade height range, and the decrease was more severe with the increase in the damage degree. This was because the increase of blade inlet angle led to an enlarged attack angle of incoming flow. This caused the airflow separation at blade leading edge, which developed rapidly on the suction surface, increasing the flow loss, and reducing the work capacity of this stage of the blade. Noticeably, due to the small curling degree of the model B rotor blade, its outlet parameters changed little from those of the original rotor.

5.3 Flow Field Analysis of Different Damage Degree Models Under Near-Stall Condition

Figure 35 depicts the relative Mach number contour comparisons for different axial sections of each model in the near-stall state. In contrast to the first two conditions, the range of the low-speed zone in the damaged blade channel was expanded, and the number of circumferential channels covered by this zone also increased. The low-speed regions in the rotor blade tip under slight, moderate,

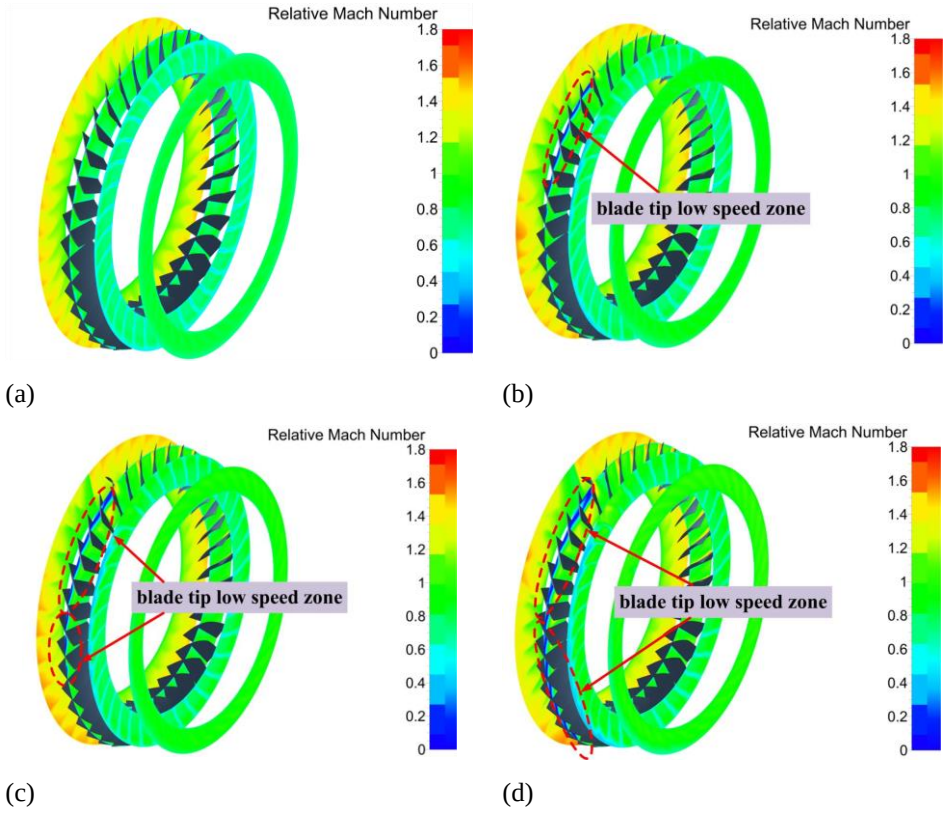

Fig. 35 Comparison of relative Mach number contours of different axial sections of each model (near-stall condition): (a) model A, (b) model B, (c) model C, and (d) model D

and severe curling conditions were expanded to 5, 8, and 12 blade channels, respectively, which were about 2.5 times larger than the numbers under the maximum-efficiency condition. The low-speed region of the rotor blade tip with severe curling occupied 1/3 of the circumferential range.

Figure 36 shows the isosurfaces with the relative Mach number of 0.25 before and after the rotor curling. The distribution position and shape of the low Mach number isosurfaces were consistent with those of the low-speed zone distributions of the axial and radial sections. This was because as the rotor continued to throttle, the downstream back pressure increased, and the attack angle of incoming flow increased, resulting in expansion of the separation zone of the damaged blade. Under the joint effect of damaged blade channel and tip leakage flow, some adjacent blades on the left side also caused flow separation at the blade tip, forming a large low-speed zone to block the flow field. With the intensifying curl degree of the blade, the circumferential scope covered by the low-speed area was also larger, and the deterioration of the rotor flow state was more significant.

Figure 37 displays the suction surface distributions of the limiting streamlines for the original blade and those with different curl degrees. As is clear from the figure, in the near-stall state, the leading edge separation zone in original blade was located near about a 35% chord length, covering the entire radial range from a 20% blade height to an 80% blade height, and the separation zone of trailing edge extended from the blade tip to root. With the intensification of blade curl degree, the separation zone near the leading edge moved from a 35% chord position to the damaged blade height at the blade leading edge. Despite the reduced radial range of leading-edge separation zone, the separation in the curled blade height range became more chaotic, which also led to the loss of flow separation gradually increasing. Due to the influence of blade leading-edge curl, the trailing edge separation zone gradually shrank within the spanwise range, and the trailing edge separation zone for damaged blade only extended from the root to the lowest height of curled blade, which indicated that the loss arising from trailing edge separation was gradually decreasing. However, given the intensified boundary layer separation in the leading edge vicinity, the flow loss increased sharply, so the total flow loss still progressively increased as the blade curling degree intensified, resulting in the deterioration of the flow state of the rotor and a significant decline in the performance, which coincided with the characteristic graph presented in Fig. 28.

To explore the influence of blade tip curl damage over the surface shock wave, we illustrate the static pressure distribution for original blade and three different damage degrees of the curled blade surface at a 95% blade height in Fig. 38. As is clear from this figure, in contrast to the original blade, the blade tip curl damage caused the shock wave position on the blade surface to appear earlier and even caused it to be pushed to the blade leading edge. This caused separation of the suction surface boundary layer behind the shock wave to occur earlier, thereby increasing the degree of flow loss. In addition, the suction surface static pressure for heavily curved blade increased sharply near the trailing edge. This was due to the blockage of the

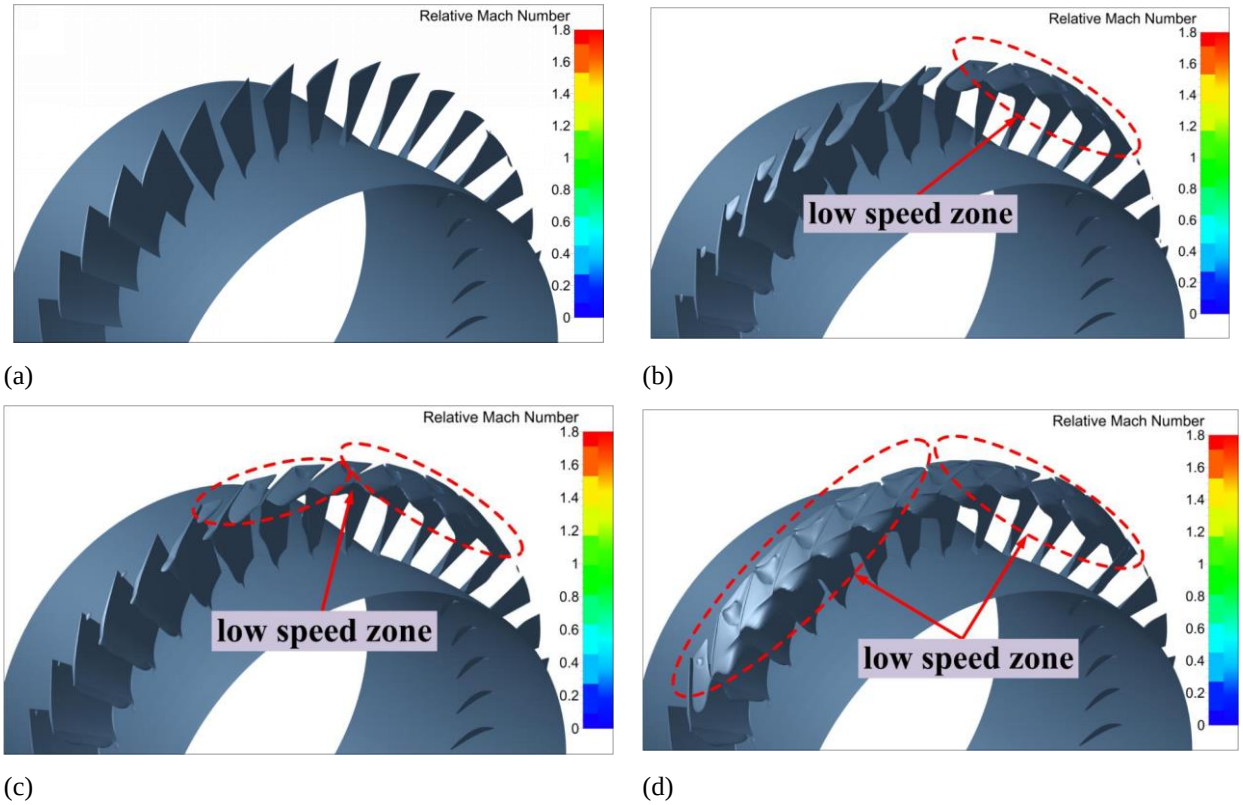

Fig. 36 Isosurfaces of different models with relative Mach number of 0.25: (a) model A, (b) model B, (c) model C, and (d) model D

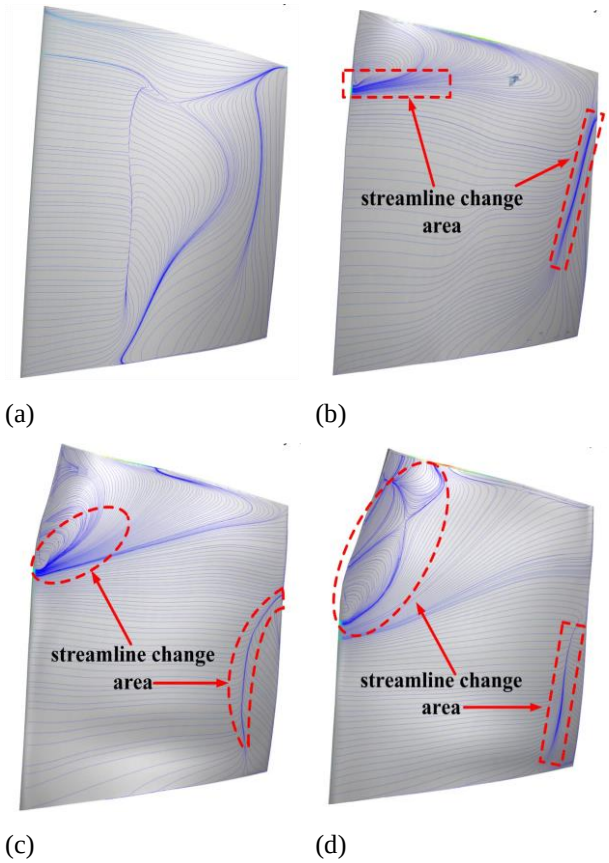

Fig. 37 Limit streamline distribution of blade suction surface: (a) original blade, (b) slightly curled blade, (c) moderately curled blade, and (d) severely curled blade

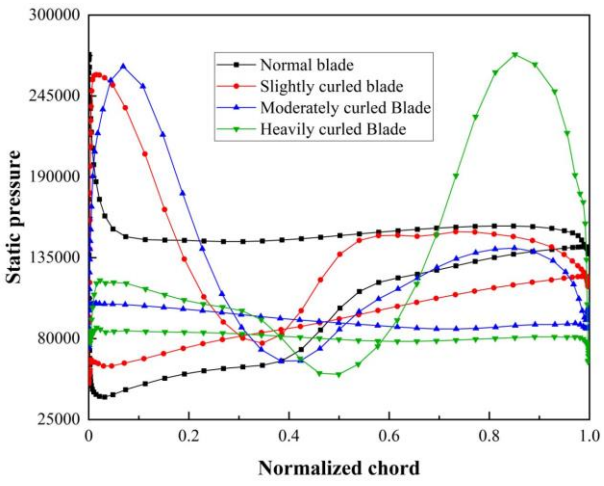

Fig. 38 Static pressure distribution along the chord length of the damaged blade and the original blade surface was changed at a 95% blade height

tip passage resulting from the curl at the blade tip leading edge, so that the airflow was squeezed to the lower part of the passage. Under the action of the high-speed centrifugal force, the lower squeezed airflow developed rapidly to the top of the passage at a 60% chord length, and the airflow on the pressure side formed a local high-pressure site under the coupled action of trailing edge backflow to the suction side.

Figure 39 shows the relative Mach number contours for various blade height sections of each model under the near-stall working scenario. In contrast to the first two

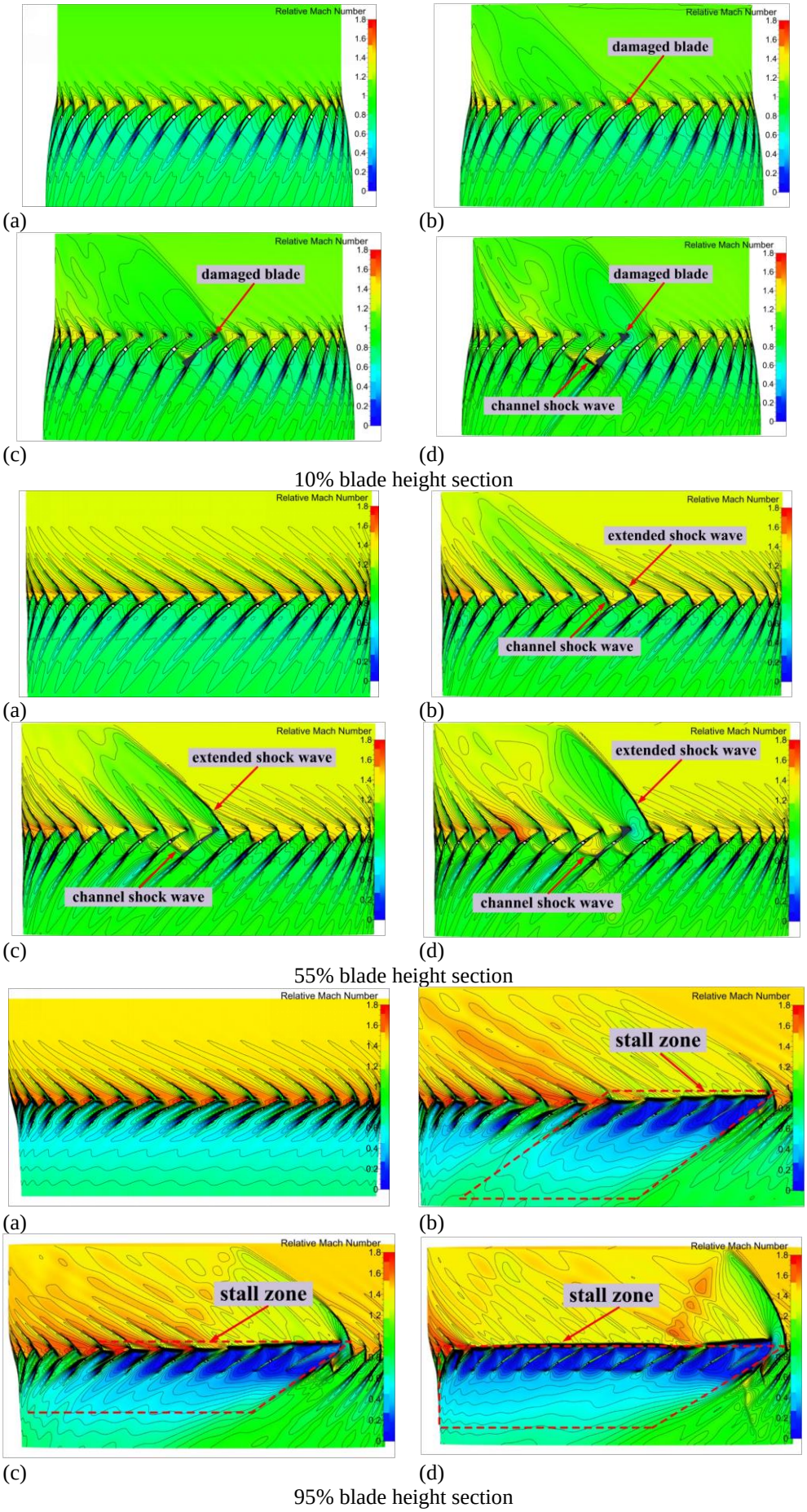

Fig. 39 Comparison of relative Mach number contours of different blade height sections of each model (near-stall condition): (a) model A, (b) model B, (c) model C, and (d) model D

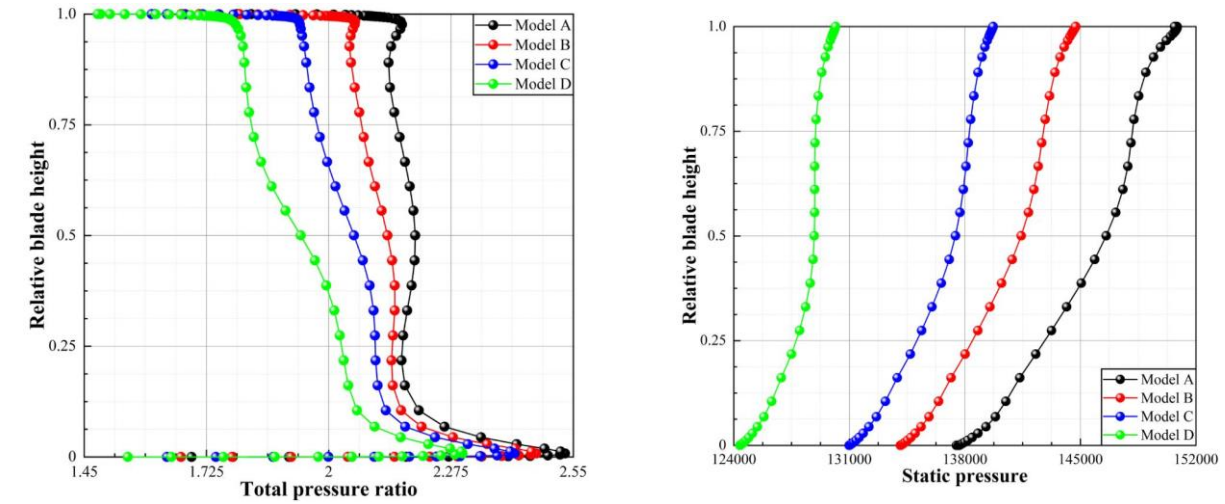

(a) (b)

Fig. 40 Rotor outlet parameters are distributed along the radial direction (near-stall condition): (a) total pressure ratio and (b) static pressure

working scenarios, due to the flow rate decline, the downstream back pressure of rotor increased, the upstream shock wave intensity increased, the Mach number after the wave decreased more drastically, and the influence of extended shock wave on the upstream range was also larger. The local high-speed zone at the leading edge of left channel inlet in the low-speed zone was more evident, and the ranges and values of these high-speed zones were significantly increased in contrast to those under the former working conditions. Besides, the low-speed region of blade tip was further expanded, and the detached shock wave at blade leading edge was pushed to a more upstream position almost perpendicular to the direction of the airflow. After the airflow passed through the normal shock wave, the Mach number decreased rapidly to subsonic speeds. Affected by the attack angle enlargement of incoming flow, the boundary layer separation began to occur at the blade suction leading edge, resulting in a low-speed region that completely covered the channel, causing blockage and affecting downstream flow.

Figure 40 shows the radial distribution of the rotor outlet parameters. Compared with the maximum-efficiency condition, the static pressure along with total pressure ratio in the whole blade height range decreased more, which still conformed to the variation trend that the more severe the damage was, the more severe the decline was. This showed that under the near-stall working scenario, the blade working ability was significantly reduced, the flow loss of the rotor increased sharply, and with the increase in the curl degree, the aerodynamic performance of the rotor deteriorated more significantly.

6. CONCLUSIONS

In this study, the mechanism through which blade damage affects the aerodynamic performances and internal flow field structures of low-speed compressors and transonic compressors were analyzed. The proposed simulation approach was validated by carrying out an aerodynamic performance experiment of the low-speed compressor. The following conclusions are drawn:

(1) The aerodynamic performance experiment and numerical simulation results of a low-speed compressor were highly consistent. At different speeds, the maximum errors of the aerodynamic performance parameters of the experimental and simulation results at the same flow rate were within ±3%, which effectively verified the rationality and effectiveness of the proposed numerical simulation approach for aerodynamic performance.

(2) After the blade was damaged, the aerodynamic properties, including the compressor isentropic efficiency and total pressure ratio, decreased significantly. The flow rate near the stall point increased, while that at the clogging point decreased, resulting in a reduced stable working range along with a significant decrease in the stability margin.

(3) The flow field assessment under each typical working condition showed that the change of blade shape caused by blade damage increased the attack angle of incoming flow, leading to local airflow separation. Its coupling with the concurrent low-speed flow was the primary factor inducing the whole rotor to enter an unstable state.

(4) Unlike the low-speed compressor, the blade damage of the transonic compressor rotor also changed the strength and position of the extended and passage shock waves, which interfered with the boundary layer separation and affected the upstream flow field of rotor. Consequently, the clogging area of internal channel of the compressor turned larger, the deterioration of the flow state became more significant, and the flow loss surged, resulting in a more severe decline in the aerodynamic performance and the transition to unstable conditions.

(5) The computational results of the transonic rotor with varying degrees of blade damage showed that as the level of blade damage increased, the rotor's ability to perform work decreased, and flow losses increased, leading to a more severe decline in the aerodynamic performance. When the rotor blades experienced minor, moderate, and severe damage, the stability margin was reduced by 8.43%, 11.56%, and 17.25%, respectively.

CONFLICTS OF INTEREST

The authors have no conflicts to disclose.

AUTHORS CONTRIBUTION

H. Sun: Methodology (equal); Software (lead); Validation (equal); Experiment (equal); Writing—original draft (lead); Writing—review & editing (equal). **Z. Wang:** Project fund acquisition (lead); Methodology (equal); Writing—review & editing (equal). **G. Luo:** Validation (equal); Writing—review & editing (equal); Supervision (equal).

REFERENCES

Barber, J. P., Taylor, H. R., & Wilbeck, J. S. (1978). *Bird impacts forces and pressures on rigid and compliant targets.* Air Force Flight Dynamics Laboratory, Air Force Systems Command.

Bohari, B., & Sayma, A. (2010). CFD analysis of effects of damage due to bird strike on fan performance. *Turbo Expo: Power for Land, Sea, and Air*, *44021*, 173-181. https://doi.org/10.1115/gt2010-22365.

Boos, P., Möckel, H., Henne, J. M., & Seimeler, R. (1998). *Flow measurement in a multistage large scale low speed axial flow research compressor.* Turbo Expo: Power for Land, Sea, and Air. American Society of Mechanical Engineers, 78620: V001T01A104. https://doi.org/10.1115/98-gt-432.

Charles, A. W., Harold, F. W., & Richard, G. S. (1995). *NASA low-speed axial compressor for fundamental research.* National Aeronautics and Space Administration, Office of Management, Scientific and Technical Information Program. https://doi.org/10.2514/6.1983-1351.

Chen, Q., Li, H., Liang, Z., Song, H., Ma, Z., & Sun, H. (2023). *Dynamic stress test of aero-engine compressor rotor blade*. Journal of Physics: Conference Series. IOP Publishing, 012033. https://doi.org/10.1088/1742-6596/2658/1/012033.

Cong, Y., Zhou, S., Wang, M., Chu, S., & Wang, Z. (2023). Effects of blade leading edge lobe top damage on pressurized air compressor performance, *Electromechanical Equipment, 40*(05), 1-9+58. https://doi.org/10.16443/j.cnki.31-1420.2023.05.001.

Guan, Y., Chen, W., & Gao, D. (2007). Current status of research on damage of aero-engine blades by foreign objects, *Journal of Aeronautics, 28(4),* 851-857. https://doi.org/10.3321/j.issn:1000-6893.2007.04.014.

Imregun, M., & Vahdati, M. (1999). Aeroelasticity analysis of a bird-damaged fan assembly using a large numerical model," *The Aeronautical Journal 103*(1030), 569-578. https://doi.org/10.1017/s0001924000064204.

Jiang, W., Ju, Y., & Zhang, C. (2017). Influence of defective blades on the aerodynamic performance of transonic compressor rotor. *Journal of Engineering Thermophysics, 38*(11), 2357-2362.

Kim, M., Vahdati, M., & Imregun, M. (2001). Aeroelastic stability analysis of a bird-damaged aeroengine fan assembly, *Aerospace Science and Technology, 5*(7), 469-482. https://doi.org/10.1016/s1270-9638(01)01122-1.

Li, L., Liu, H., & Li, P. (2018). Aerodynamic effects of blunt leading edge of compressor blade on boundary layer, *Propulsion Technology, 39*(2), 299-307. https://doi.org/10.13675/j.cnki.tjjs.2018.02.007.

Li, P., Zuo, H., Xiao, W., Guo, Z., & Yuan, Z. (2024). Research and prospect of aero-engine blade damage and its repair technology, *Journal of Aeronautics*, 1-27. https://doi.org/10.7527/S1000-6893.2023.29635.

Li, Y., & Sayma, A. (2012). *Effects of blade damage on the performance of a transonic axial compressor rotor.* Turbo Expo: Power for Land, Sea, and Air, American Society of Mechanical Engineers, 44748, 2427-2437. https://doi.org/10.1115/gt2012-68324.

Li, Y., & Sayma, A. (2015). Computational fluid dynamics simulations of blade damage effect on the performance of a transonic axial compressor near stall. *Proceedings of the Institution of Mechanical Engineers, Part C: Journal of Mechanical Engineering Science, 229*(12), 2242-2260. https://doi.org/10.1177/0954406214553828.

Liu, S., Chen, W., Wang, Z., & Luo, G. (2022). Numerical simulation of aerodynamic performance of pressurized airplanes containing bird strike deformed blades. *Aeroengine 48*(02), 7-13, https://doi.org/10.13477/j.cnki.aeroengine.2022.02.002.

Lu, J. (2017). *Experimental and numerical simulation study on aerodynamic performance of fan damaged by bird impact*, Shanghai, Shanghai Jiaotong University.

Lu, J., Qiang, X., Teng, J., & Yu, W. (2017). Airworthiness compliance study of aerodynamic performance of bird impact damaged fan. *Journal of Shanghai Jiao Tong University, 51*(08), 932-938. https://doi.org/10.16183/j.cnki.jsjtu.2017.08.006.

Muir, E. R., & Friedmann, P. P. (2013). *Unsteady aerodynamic analysis of a bird-damaged turbofan.* 54th IAA/ASME/ASCE/AHS/ASC Structures, Structural Dynamics, and Materials Conference, 1773. https://doi.org/10.2514/6.2013-1773.

Muir, E. R., & Friedmann, P. P. (2014). *Aeroelastic response of bird-damaged fan blades using a coupled CFD/CSD framework*. 55th AIAA/ASMe/ASCE/AHS/SC Structures, Structural Dynamics, and Materials Conference, 0334. https://doi.org/10.2514/6.2014-0334.

Muir, E. R., & Friedmann, P. P. (2016). Forced and aeroelastic responses of bird-damaged fan blades: A

comparison and its implications. *Journal of Aircraft 53*(2), 561-577. https://doi.org/10.2514/1.c033424.

Qin, L., Zhang, H., Zhou, L., He, W., & Wu, Y., (2022). Effects of blade tip dropout on aerodynamic performance of transonic compressor. *Propulsion Technology*, *43*(10), 87-97, https://doi.org/10.13675/j.cnki.tjjs.210346.

Reid, L., & Moore, R. D. (1978). *Design and overall performance of four highly loaded, high-speed inlet stages for an advanced high-pressure-ratio core compressor*. NASA-TP-1337.

Reid, L., & Urasek, D. C. (1973). Experimental evaluation of the effects of a blunt leading edge on the performance of a transonic rotor, 199-204. https://doi.org/10.1115/1.3445723.

Suder, K. L. (1996). *Experimental investigation of the flow field in a transonic, axial flow compressor with respect to the development of blockage and loss*, Case Western Reserve University.

Sun, L., Zhang, Z., Zhang, K., Zheng, B., Shi, T., Zhang, G., & Gao, D. (2024). Study on the effect of external impact damage on aero-engine fan blades, *Mechanics Quarterly*, *45(01)*, 99-109. https://doi.org/10.15959/j.cnki.0254-0053.2024.01.008.

Tang, J., Zhong, Z., Lu, X., & Wang, L. (2023). Study of the effect of a blade tip notch damage on the aerodynamic performance of transonic compressor rotors, *Fluid Dynamics*, *58*(8), 1623-1639. https://doi.org/10.1134/s0015462823600803.

Venkatesh, S., Suzuki, K., Vahdati, M., Salles, L., & Rendu, Q. (2020). *Effect of geometric uncertainty on a one stage transonic compressor of an industrial gas turbine.* Turbo Expo: Power for Land, Sea, and Air. American Society of Mechanical Engineers, 84065: V02AT32A078. https://doi.org/10.1115/1.0002996v.

Yang, J. (2014). *Research on fan blade bird impact response and aerodynamic performance analysis method of damaged fan*. Nanjing, Nanjing University of Aeronautics and Astronautics.

Yang, X., Li, A., Cao, B., Shen, H., & Liu, S. (2021). Numerical simulation study on the bird strike performance of fan/booster stage of aero-engine with large-containment-channel-ratio. *Gas Turbine Technology*, *34*(03), 21-27. https://doi.org/10.16120/j.cnki.issn1009-2889.2021.03.003.

Zhang, C., Hu, J., Wang, Z., Yin, C., & Yan, W. (2015). Numerical study of three-dimensional optimization of rotor blades for low-speed axial-flow compressor. *Journal of Aerodynamics*, *30*(02), 483-490. https://doi.org/10.13224/j.cnki.jasp.2015.02.028.

Zhao, Z., Wang, L., Lu, K., Li, Y., Chen, W., & Liu, L. (2020). Effect of foreign object damage on high-cycle fatigue strength of titanium alloy for aero-engine blade, *Engineering Failure Analysis*, *118*, 104842. https://doi.org/104842.10.1016/j.engfailanal.2020.104842.